Additive Manufacturing 67 (2023) 103489

Contents lists available at ScienceDirect

Additive Manufacturing

journal homepage: www.elsevier.com/locate/addma

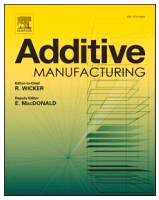

Research paper

Development of a process optimization framework for fabricating fully dense advanced high strength steels using laser directed energy deposition

M.W. Vaughan [a], M. Elverud [a], J. Ye [b], R. Seede [a], S. Gibbons [c], P. Flater [d], B. Gaskey [d], R. Arroyave [a,b], A. Elwany [b], I. Karaman [a,*]

[a] Department of Materials Science and Engineering, Texas A&M University, College Station, TX 77843, USA
[b] Wm Michael Barnes '64 Department of Industrial and Systems Engineering
[c] Operations Division, AFWERX, Eglin Air Force Base, FL 32542, USA
[d] Fuze & Warhead Research Branch, Air Force Research Laboratory, Eglin Air Force Base, FL 32542, USA

ARTICLE INFO

Keywords:
Direct Energy Deposition Laser Beam (DED-LB)
Additive Manufacturing
Martensitic Steels
Printability Maps
Process Optimization

ABSTRACT

Novel advanced high-strength steels have recently gained renewed interest as engineering materials for various industries due to their low cost and high strength and toughness. One such steel is the recently developed martensitic AF9628 steel which exhibits ultimate tensile strengths (σ_{UTS}) approaching 2 GPa with notable (~10 %) elongation to failure (ε_f). Given its high performance and low cost, AF9628 is a potential candidate for fabricating large, fully dense complex parts using the additive manufacturing (AM) technology known as directed energy deposition (DED). DED offers unique advantages over powder bed fusion AM due to its relative scalability, applicability for part repairs, and potential for producing compositionally and functionally graded parts. Yet, using DED for printing fully dense new alloys has often proven challenging due to its complex physics at the melt pool and many processing parameters that require simultaneous optimization. Thus, there is a pressing need for developing a comprehensive, machine-agnostic, and straightforward DED process optimization framework that guides the appropriate selection of printing parameter levels to successfully print new alloys to full part density (i.e., >99 %). Such a DED process optimization framework has been developed and is presented herein, which is easily applicable to other materials. It produced nearly fully dense (>99 %) builds of AF9628 with excellent and consistent mechanical performance levels ($\sigma_{UTS} > 1.2$ GPa, $\varepsilon_f > 10$ %) across parameter sets, which is a feature of the unique dilution, hatch spacing, and layer thickness criteria developed for the framework. Lower strength levels than those of wrought AF9628 were partly attributed to decarburization during printing, indicating the need for proper selection of the initial carbon content in steel powders to arrive at the targeted carbon levels and mechanical properties in the DED fabricated parts. The ability of decarburization by controlling DED process parameters can enable fabrication of parts with location specific properties.

1. Introduction

Advanced high-strength steels (AHSSs) are increasingly important in various industries requiring exceptional mechanical performance under extreme conditions [1–3]. For instance, Space-X uses a proprietary AHSS for its Starship design because their steel is capable of maintaining high strength both at cryogenic temperatures (upon leaving the Earth's atmosphere) and elevated temperatures (upon re-entry through the Earth's atmosphere) [1]. Additionally, defense applications typically require high-performance steels for armors [2] or ballistic penetrants [3], where the dynamic stress state imposed on the material is extreme. AHSSs are also broadly applicable for light-weighting in the various transportation industries for fuel conservation, a result of their reasonable cost and higher specific strengths, and overall high strengths compared to competing alloys [4]. More generally, one of the main objectives of current research on AHSSs is to achieve high performance, particularly high toughness and strength, while lowering alloying and material fabrication costs. Therefore, such alloys are classified as third-generation AHSSs, as they perform better regarding strength and toughness than first-generation AHSSs and are less expensive than second-generation AHSSs [5]. Furthermore, the low-cost/high-strength of third-generation AHSSs allows them to be used more broadly in a

* Corresponding author.
E-mail address: ikaraman@tamu.edu (I. Karaman).

https://doi.org/10.1016/j.addma.2023.103489
Received 29 December 2022; Received in revised form 25 February 2023; Accepted 7 March 2023
Available online 11 March 2023

variety of applications, such as within car frames for vehicular light-weighting [6].

Presently, interest in additive manufacturing (AM) of AHSSs has grown significantly due to their high versatility and excellent mechanical properties. One such AHSS, AF9628, is an inexpensive, high-strength low alloy (HSLA) fully martensitic steel invented by Abrahams et al. [7] in 2016. In 2020, Seede et al. [8] developed an easily implementable process optimization framework for laser powder bed fusion (L-PBF) AM of AF9628, which produced excellent (> 99 %) density with superb mechanical properties (yield strengths (σ_{Yield}) > 1.0 GPa, ultimate tensile strength (σ_{UTS}) > 1.4 GPa, elongation to failure (ε_f) > 10 %). This L-PBF process optimization framework [9] enabled printing parts repeatedly to near full density (>99 %) with properties comparable to the wrought condition in many different alloys [10–19].

Due to L-PBF's rapid cooling rates (10^4-10^6 K/s [20]), it creates a refined, fully martensitic microstructure in AF9628 [8,10] which is ideal for achieving high strength/toughness combinations. However, part sizes and build rates attained using L-PBF are below the level of practical expectations for many defense applications. Alternative AM techniques such as Laser Beam Directed Energy Deposition (DED-LB) [21], are capable of printing larger part sizes at faster build rates than L-PBF [22,23]. Despite slower cooling rates in DED-LB (10^2-10^4 K/s [20]) compared to L-PBF (caused by the former's higher power levels, slower scan speeds, and larger laser beam diameters), DED-LB offers key advantages in addition to its larger part sizes and faster build rates. In particular, it can be highly efficient, capable of utilizing as much as 80–90 % of the blown powder while printing [24–26], thereby printing near net shapes while requiring much less powder to be recycled in between prints – in stark contrast to L-PBF. Additionally, DED-LB can be used to repair parts [27,28] and print multi-materials by systematically adjusting powder compositions during printing by changing the mixing ratios of different powders from various powder feeders, yielding parts with functionally graded properties [29–32].

Currently, however, printing nearly fully dense parts with DED-LB is challenging due to the lack of sufficient understanding on how different process parameters influence defect formations, a result of the complex physics at the melt pool where blown metallic particles arrive at the energy source and are simultaneously melted and welded into the substrate underneath [25]. Here, the dynamics of blown powder and their interaction with the laser in DED-LB starkly contrast with the powder's static state in L-PBF [29]. Therefore, there is an urgent need to develop a simple process optimization framework for DED-LB that enables the fabrication of nearly fully dense AHSS parts with refined microstructures and high strength levels.

Any simple process optimization methodology for melt-based AM techniques should include a way to predict/measure melt pool dimensions to identify the regions in the process parameter space that would lead to melt-pool-induced porosity due to keyholing, lack of fusion, and balling. However, the melt pool physics in DED-LB are very complicated compared to L-PBF. For example, in L-PBF, coupled laser power (P, W) and scan speed (V, mm/s) limits allowing for powder melting while avoiding defects can be approximated via simple welding-based heat transfer/melting models, such as the Eagar-Tsai model [33], where melt pool dimensions can be accurately predicted after proper calibration of model parameters. However, DED-LB's parameter space is minimally three-dimensional, consisting of laser power, scan speed, and mass flow rate. Here, the complex nature of coupled powder, gas, laser, and melt pool interactions [29,34–38], where mass deposition is dynamic not static, makes simple welding models inaccurate in predicting melt pool geometries and defects. More complex, machine- and material-specific models and approaches are required [25,29,34–36,38,39]. Consequently, an alternative, largely empirical approach appears to be, presently at least, more practical for creating a machine- and material-agnostic DED-LB Process Optimization Framework.

Early studies on optimizing powder-fed laser printing can be found in the cladding literature for different metal systems [25,40–45]. These studies are fundamentally useful to understanding the DED-LB process, although their printing criteria are not directly applicable to DED-LB since the objectives in laser cladding – protecting a substrate's surface by the cladded metal coating while imposing minimal heat input to the substrate – differ from DED-LB's objective of building fully dense bulk components. Examples of cladding criteria can be found in the work by Steen et al. [40], who suggested hatch spacings between 50 % and 70 % of the single-track width, a single-track width-to-height aspect ratio below 5, and a wetting angle above 134° for maximal surface smoothness. Similarly, Balu et al. [45] identified a hatch spacing at 66 % of the width as ideal for a single layer's smoothness. Such cladding criteria are informative but can become quite specific and less generalized to other applications and material systems. Also, they do not consider the height and depth of single tracks in the formulation of their hatch spacing criteria. Since cladding is typically applied as a single layer [40,41,45,46], the need for optimizing layer thickness settings is often neglected also.

In contrast, more recent studies on DED-LB process optimization have often been challenged by the abundance of printing parameters simultaneously requiring fine tuning. Thus, many simplified the problem by examining only two dimensions of the minimally three-dimensional (laser power, scan speed, and mass flow rate) process parameter space at a time [30,47,48]. Others investigated the three-dimensional space [24,49–54] or studied the effects of additional process parameters, such as shielding gas flow rates [55,56] and laser focal height [57], with less emphasis on the effects of different combinations of power, scan speed, and mass flow rates. Additionally, some investigated the effects of combined parameters such as linear energy density [52,58], mass deposition rate [52], or more complex parameters [24,54] on predicting single-track geometries. Many also reported on the effects of DED-LB in producing thin-walled structures by vertically stacking single tracks [26,52,56,57,59,60], but this approach negates the need for setting optimal hatch spacing and layer thickness levels.

Regardless of the type of study, most studies, while useful, typically did not completely prove the effectiveness of generated DED-LB printability maps, as printing multi-layer parts, measuring their densities, and conducting tensile testing afterward were often not shown together for validation purposes [24,30,45,49–54,56,61–64]. Additionally, in contrast to L-PBF where a part's dimensional height accuracy is easily ensured by setting layer thickness as a function of the powder size [8], setting layer thickness for good dimensional accuracy in DED-LB is more difficult due to the dynamic mass flow rate [65]. Yet, clear criteria for setting hatch spacing and layer thickness in DED-LB to produce fully dense parts were often not provided in past studies, e.g., [21,24,47,50,53,58,62,66–68].

Currently, it is rare to find studies that connected single-track printability maps to printing bulk parts to full density and good tensile mechanical properties. As such, often the general approach for printing fully dense parts via DED-LB involves either outsourcing printing to a vendor or, if printing internally, conducting small screening experiments that identify moderate power, speed, and mass flow rate settings followed by the use of somewhat arbitrary, conservative hatch spacing and layer thickness levels which do not comprehensively consider single-track geometries (i.e., track height, depth, and width) in their formulations. Therefore, such strategies are neither systematic nor robust in preventing deleterious lack of fusion between layers, inter-track porosity, or geometrical inaccuracy. Collectively, such criteria are also difficult to apply due to their relative incongruity.

With this in mind, it remains crucial to connect the current knowledge available in the literature, ranging from laser cladding to L-PBF to DED-LB studies, to develop a DED-LB Process Optimization Framework. Therefore, the present study does exactly this, demonstrating that a straightforward, repeatable, largely machine- and material-agnostic DED-LB framework can be constructed empirically and applied

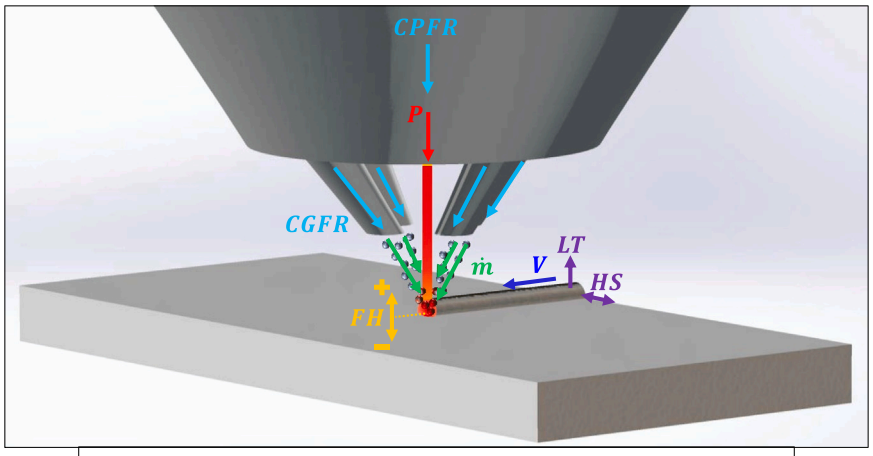

Laser Beam Directed Energy Deposition (DED-LB)

Print Parameters
- Laser Power (***P*** **[W]**)
- Scan Speed (***V*** **[mm/s]**)
- Mass Flow Rate (***ṁ*** **[g/s]**)
- Center Purge Flow Rate (***CPFR*** **[L/min]**)
- Carry Gas Flow Rate (***CGFR*** **[L/min]**)
- Laser Focal Height (***FH*** **[mm]**)
- Hatch Spacing (***HS*** **[mm]**)
- Layer thickness (***LT*** **[mm]**)

Powder Characteristics
- Composition
- Physical Properties: Melting point (T_m), Reflectivity (η), Density (ρ), Relative Enthalpy (ΔH) …
- Powder Size [μm]
- Powder Shape (Spherical, Plate) from Atomization Process (Water, Gas)

Fig. 1. A schematic showing the printing of a single-track via laser beam directed energy deposition (DED-LB). The track's characteristics are dependent upon various print parameters and powder characteristics, as shown, which make printing fully dense metallic parts fairly complex. Note that for printing multi-track and multi-layer builds, additional printing parameters – layer thickness (LT) and hatch spacing (HS) – must be set appropriately to achieve high density via strong fusion between both adjacent single-tracks and each subsequent layer printed.

directly to consistently achieve fully dense builds of AF9628 martensitic steel. Here, the novelty of this work lies in its comprehensive nature, as it provides all the essential steps needed to print a new metal alloy system to full density and consistent mechanical performance levels via DED-LB. Process optimization proved substantially different for DED-LB versus the previous L-PBF framework study [8]; for DED-LB, new challenges and complications arose from its additional parameters (discussed in Section 3.1) which, in particular, were related to the imposed dynamic mass flow rates and layer thickness. The presented findings demonstrate clearly that one cannot simply apply the L-PBF process optimization framework directly to DED-LB, as different mass flow rate settings produced widely disparate printability regions in the process parameter space.

While not shown and currently unpublished, the DED-LB Process Optimization Framework presented herein has been successfully applied by the authors to a wide array of other materials, such as 316 L stainless steel, GR91 ferritic martensitic steel, pure vanadium, VCrTi alloys, VCrAl alloys, and FeCrAl alloys (with high Al content), producing > 99 % density without difficulty. This was possible not because these materials are easy to print – in fact, they were often very difficult to print due to their oxygen sensitivity, different crystal structures, or brittle ordered phases such as B2 and L12 – but because the presented framework was effective across material systems. This study should therefore help the research community meet its needs for material-specific optimization [31], enabling the printing of new materials to near full density/net shape while promoting the realization of DED-LB's potential for functionally graded material design and development as a mainstream AM technology.

2. Materials and methods

2.1. AM platform and AF9628 powder characteristics

In this study, a LENS MR-7 DED-LB machine from Optomec, Inc. was utilized for printing. Ultrahigh-purity argon (>99.995 %) was circulated within the chamber and powder lines to prevent oxidation. The machine uses a four-nozzle system that centers the powder stream onto the substrate for material delivery and possesses multiple powder feeders, called Hoppers. These feeders supply powder through the nozzles at mass flow rates controlled by the set revolutions per minute (RPMs) of a motorized spinning wheel within the feeder, which pushes powder into the lines where the carrying gas (Ar) feeds it through the four nozzles. For consistency, the same Hoppers and locations were used at all times for all experiments herein, from mass flow rate calibration curves, which determine mass flow rate as a function of the hopper feeder wheel RPMs, to printing single-tracks and multi-layer builds. Hopper feeder wheel speed can be set from 0 to 10 RPMs.

As illustrated in Fig. 1, the DED-LB process has many important printing parameters that influence the physics at the melt pool and, thus, the resultant print aesthetics, densities, microstructures, compositions, and, ultimately, mechanical properties. Consequently, it is essential to understand the effects of these parameters on part characteristics before printing. In particular, when printing bulk samples via DED-LB, one must consider how to adjacently space powder tracks and how to vertically displace the printing head for each layer. To clarify, the distance between adjacent tracks for the same layer is defined as hatch spacing (*HS, μm*), and layer thickness (*LT, μm*) is defined as the vertically upward z-displacement in between layers, set by the user. These additional print parameters affect the interlayer and intertrack porosity and, therefore, must be appropriately set to ensure maximum density. Scan strategy can be another critical parameter for producing different structural and microstructural features; in this work, a ± 90° scan strategy was used between layers for all experiments.

The LENS MR-7 uses a 1 kW IPG laser with a CVI PLCX-50.8–72.1-UV-1064 customized optical lens that has a 160.4 mm focal length and a beam size approximately 600 μm in diameter. The laser focal height (*FH, mm*) was alternated between + 5.08 and − 5.08 mm in this study, where the laser focal plane was located either 5.08 mm above the substrate surface (leading to a diffuse laser) or 5.08 mm below the substrate surface (i.e., a non-diffuse laser). Wrought AF9628 in the normalized condition (forged, austenitized at 1010 °C for 2 h, and air-cooled) was used as substrates for all experiments to match the chemistry between the substrate and powder, thereby promoting optimal fusion and maximal bond strength [40]. These substrates were surface ground

Table 1
Comparison of the AF9628 martensitic steel compositions under a variety of conditions (from left to right): patent standards [7], wrought AF9628 in the Baseline condition [4], the AF9628 DED-LB powder and as-printed conditions of the present work, and, finally, the L-PBF powder and as-printed conditions [10]. Chemistries were determined using Inductively Coupled Plasma – Atomic Emission Spectroscopy (ICP-AES).

			DED-LB (current study)		L-PBF [10]	
Elements (wt. %)	Standards [7]	Baseline [4]	Powder	As-Printed	Powder	As-Printed
Fe†	Balance	93.14	93.08	92.26	93.29	93.53
Ni	< 3.00	1.03	1.02	0.79	1.03	0.97
Cr	2.00–3.00	2.76	2.87	4.70	2.69	2.61
Mo	0.50–1.50	0.97	1.00	0.75	0.92	0.92
Si	< 1.25	1.05	1.01	0.78	1.01	0.90
Mn	< 1.00	0.57	0.58	0.42	0.55	0.65
C††	0.24–0.32	0.29	0.25	0.16	0.26	0.23
V	0.05–0.35	0.04	0.05	0.04	0.07	0.09
Cu†††	< 0.15	0.15	0.14	0.10	0.14	0.08
Al†††	< 0.025	–	0.01	0.01	0.02	0.01
Co†††	–	–	–	–	0.02	0.01

†Determined by difference
††Determined via combustion-infrared absorbance
†††Impurity element

before printing, and substrate temperatures were directly measured with several thermocouples. Multi-layer prints were paused by the operator when substrate temperatures became excessive (>150 °C) to allow for part cooling and minimize tempering effects, which reduce strength in martensitic steels.

Oxygen levels were monitored to remain below 50 parts per million (ppm). Analog knobs enable the user to control Ar flow rates (pressures) through the center purge and the powder-carrying lines. Here, the center purge flow rate (*CPFR*, L/min) protects the laser optics from potential damage induced by molten powder and can be set between 0 and 30 L/min; a conservative value of 28 L/min was chosen for all experiments to better protect the laser optics. In contrast, carrier gas flow rate (*CGFR*, L/min) ranges from 0 to 10 L/min; the authors found that 3 L/min worked well to minimize surface roughness in bulk samples in this machine. Moderately low *CGFR*s allow particles to arrive at lower velocities and higher temperatures to the melt pool, optimizing thermal transfer while preventing balling defects that can occur from rapid cooling [56,69]. To mitigate the effects of moisture on powder flowability, which can cause the powder to stick and clump within the lines, clogging them, all powder was placed in a beaker and dried on a hotplate, in the glovebox under an Ar atmosphere at 103 °C for 12 h before printing. 103 °C was used rather than 100 °C to promote evaporation for all powder in the beaker, regardless of vertical distance from the hot plate. Powder mass flow was stabilized for 45 s before each print. The AF9628 powder used for printing in this study was Ar gas atomized by Nanoval GmbH & Co. KG in Berlin, Germany. Its composition is shown in Table 1, which was determined by Inductively Coupled Plasma – Atomic Emission Spectroscopy (ICP-AES) where accurate C content required analysis via combustion-infrared absorbance. Comparable measurements of AF9628 under different processing conditions are also shown and will be discussed later in more detail. The powder was characterized before printing, first being imaged via scanning electron microscopy (SEM) to determine its shape and morphology (Fig. 2a-b). The powder typically appeared spherical, a consequence of the gas atomization process. Second, its size distribution was measured three independent times to ensure accuracy with a Horiba Partica LA-960S Laser Diffraction Particle Size Analyzer with a SolvoFlow Pump System. The particle sizes ranged from 30 to 120 μm (Fig. 2c). Finally, the mass flow rate ($\dot{m}, mg/s$) of the AF9628 powder was calibrated by blowing powder through the nozzles at varied hopper feeder wheel RPMs into bags; the bags' weight changes were then measured as a function of blown time (1 min) and RPMs (from 2 to 6), to establish the following linear relationship:

$$\dot{m}(mg/s) = -10.9 + 29.5 * RPMs \quad (1)$$

between *RPMs* and $\dot{m}$ of the AF9628 powder. The experimental data and linear fit are shown in Fig. 2d.

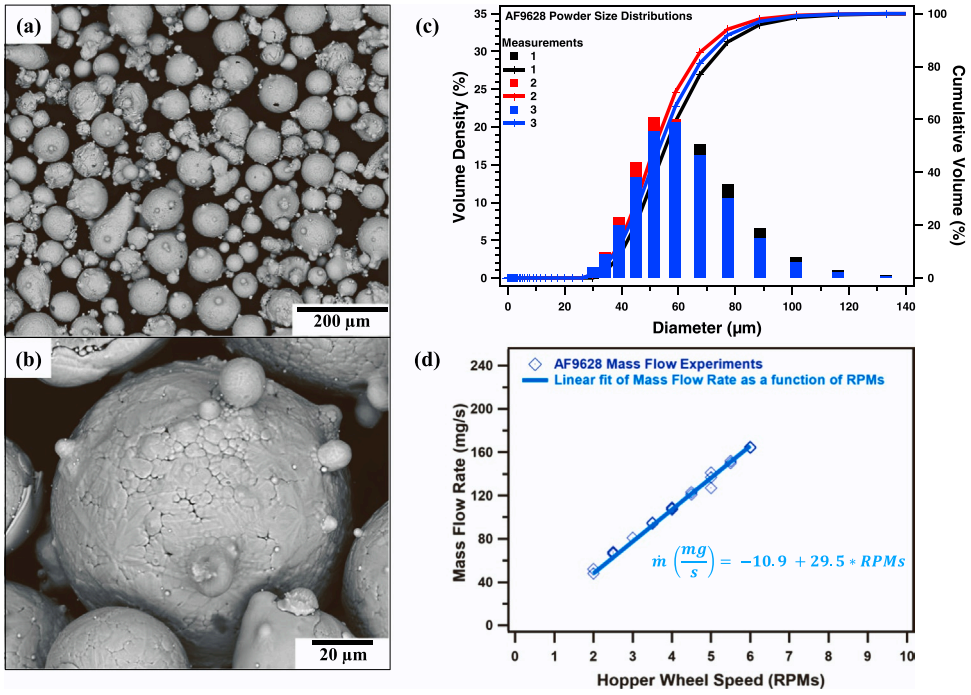

Fig. 2. Powder characterization steps for DED-LB printing, displaying (a-b) SEM of AF9628 powder particles showing general spherical morphology, (c) particle size distribution measurements confirming that the powder sizes are normally distributed and range about 30–120 μm in diameter, (d) experiments for calibrating the mass flow rate ($\dot{m}, mg/s$) of AF9628 powder as a function of the LENS MR-7® hopper feeder wheel (*RPMs*).

2.2. Microstructural and mechanical characterization experiments

Before continuing with the DED-LB framework development, a few notes regarding DED-LB printed sample geometries, density measurements, mechanical testing procedures, and metallographic imaging experiments are included for completeness. Wire electrical discharge machining (EDM) was used for all sample cutting. Printed powder single-tracks were 12.7 mm long and sectioned twice to observe two cross-sections per print parameter set. Printed cubes for density measurements were 10 mm × 10 mm in cross-sectional area with variable heights, all set to exceed 4.5 mm to provide sufficient volume for reliable density measurements. Archimedes cube density measurements followed the ASTM B962–15 standard. These cubes were then cut in half at their centers through the entire height to observe any optical porosity, which was measured by analyzing the pore area fractions. Tension blocks were 10 mm × 32 mm in cross-sectional area by 10 mm in height, and flat "dog-bone" tensile samples were cut along the horizontal direction, with gage sections of 8 mm × 3 mm × 0.75 mm. Tensile testing was conducted on an MTS test frame at a strain rate of 5×10^{-4} s^{-1} with an MTS extensometer directly attached to the gage section of the samples.

A Keyence VH-X digital microscope equipped with a VH-Z100 wide-range zoom lens was used for optical imaging. Both an FEI Quanta-600 SEM and a Tescan FERA-3 Model GMH Focused Ion Beam SEM were used for electron microscopy (i.e., for secondary electron (SE) imaging and electron backscattered diffraction (EBSD) mapping, respectively). Single-track cross-sections were ground and polished to a final step of 1 μm diamond paste followed by etching with nital (4 % nitric acid, 96 % methanol by volume) to reveal single-track geometries and the martensitic microstructure. This etching step was skipped for the AF9628 cubes to avoid categorizing any etchant-induced pores as porosity formed during printing. EBSD images were taken on the tensile samples at the center of their gage sections before deformation. These samples were polished to a final step of 0.04 μm using colloidal silica. EBSD scans utilized a step size of 300 nm and magnification of 1000X to reveal prior austenite grain (PAG) boundaries and martensite lath morphologies. Martensite laths were identified at misorientation angles greater than 5° in EBSD scans. ImageJ was used to calculate martensite individual lath areas from which martensite lath equivalent diameters were then calculated. A minimal lath area of 1 μm^2 was imposed to reduce error from experimental noise. PAG boundaries were identified at misorientation angles between 15° and 48° in EBSD following the procedures introduced in [4,8,10,70]. Once identified, approximate PAG diameters were measured manually and are described as the equivalent diameters in the text. To measure single-track surface roughness, a Keyence® VK9700 violet laser scanning confocal microscope (VLSCM) was utilized.

3. Constructing the DED-LB process optimization framework via single-track analysis

3.1. Single-tracks geometries as function of process parameters

The relevant printing parameters and their ranges for the LENS MR-7 were as follows: P [≤ 1000 W], V [≤ 17 mm/s], $\dot{m}$ [≤ 300 mg/s (an approximation for steels, as this is dependent on hopper feeder wheel RPMs which can be set between 0 and 10)], FH [-10 mm to +10 mm], *CPFR* [≤ 30 L/min], and *CGFR* [≤ 10 L/min]. Together with *HS* and *LT* parameters, there are, in total, eight printing parameters for the LENS MR-7 to optimize in order to print porosity-free bulk samples. Following the discussion in Section 2.1, the parameter space was reduced by setting *CPFR* and *CGFR* constant at the levels of 28 L/min and 3 L/min, respectively. Consequently, the levels for the single-track parameters studied are listed as follows: five P levels (200, 250, 300, 350, and 400 W), three V levels (4.2, 6.4, and 8.4 mm/s), three $\dot{m}$ levels (77.6, 107.1, and 136.6 mg/s), and two *FH* levels [+ 5.08, − 5.08 mm]. Fig. 3

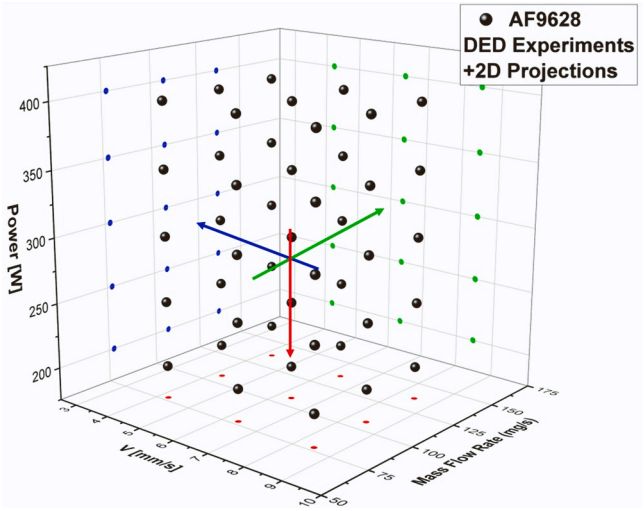

Fig. 3. Visualization of the parametric experimental plan for printing single-tracks, which sampled the P-V-$\dot{m}$ space at 5 levels of power (P), 3 levels of speed (V), and 3 levels of mass flow rate ($\dot{m}$). Note that this experimental set was repeated for two different focal heights (*FH*s), with the focal plane at 5.08 mm above and 5.08 mm below the substrate; thus, 90 (= 5 ×3 x 3 ×2) single-tracks were printed in total. The blue dots indicate the P-$\dot{m}$ points studied, the red dots indicate the V-$\dot{m}$ points studied, and the green dots indicate the P-V points studied.

presents this parametric study for printing single tracks across the quaternary space, where the projections onto the 2D parameter spaces (i.e., the P-V, V-$\dot{m}$, and P-$\dot{m}$ planes) are indicated with green, red, and blue dots, respectively. Given that the parameter values studied required 90 (5 ×3 ×3 ×2 = 90) experiments, these 45 single-track experiments were repeated for both *FH*s, for a total of 90 AF9628 single-tracks printed.

Single tracks provide a plethora of valuable information, as shown in Fig. 4, with minimal powder use. Optical and SE microscopy of the top surfaces (Fig. 4a and c) can identify qualitative features, such as cracks, spatter, or oxidation, indicative of single-track uniformity or damage. More quantitatively, as illustrated in Fig. 4b, metallographic images of etched single-track cross-sections provide details regarding single-track geometry, i.e., height (H), width (W), and depth (D) as well as area of the clad (A_{Clad}), area of the melted substrate (A_{Melt}), and the angle of wetting (α). Surface roughness (SR, R_q) of the tracks (Fig. 4d) can be used for quantifying track geometric consistency above the substrate as well as the amount of powder spattering. As shown later, H, W, and D are important parameters for the development of the hatch spacing and layer thickness criteria, so their measurements were made carefully. Specifically, W was confined to the part of the track that had some depth to it. Thus, spattering at the single-track perimeter was not included in the W calculations. Likewise, because spattering caused fluctuations in single-track H, spattered particles were not included in the cross-sectional H measurements either. This method was followed to allow for the spattered particles to be melted and fused into the material upon the deposition of adjacent tracks and layers, as it prevented the use of too high hatch spacing or layer thickness settings. Note also that H and D were measured at their extremums by convention, which typically occurred at the track centers. With this in mind, connecting the print parameters (P, V, $\dot{m}$, *FH*) to the geometric features enabled the establishment of a variety of functional relationships, which enabled a better understanding of the effects of different processing parameters on the printing performance of the DED-LB machine.

As discussed in the following sections, the *FH* values (−5.08 and +5.08 mm) did not significantly influence the single-track geometries. This fact enabled the establishment of general relationships between print parameters and single-track geometries, as illustrated in detail in

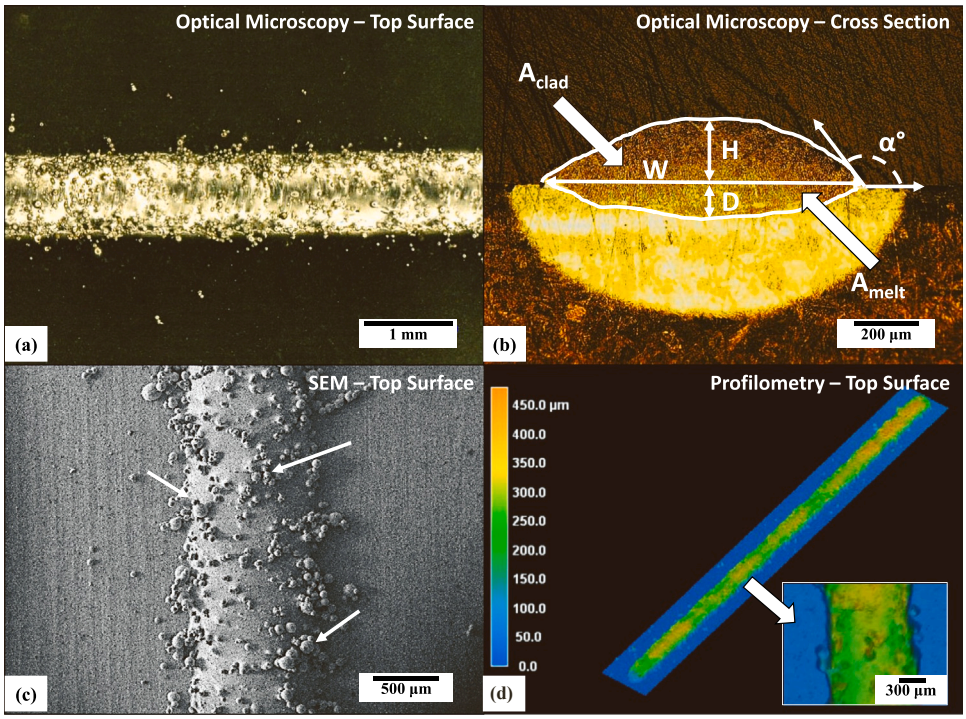

Fig. 4. Single-tracks at given *P-V-ṁ* settings provide a plethora of valuable information. In (a) and (c), optical microscopy and SEM of the track surfaces provide details on a track's qualitative defects, which can include particle spattering effects (arrows), or cracks and waviness (not shown). More quantitative characterization is done by analyzing single-track cross-sectional areas, as shown in (b), where track height (H), width (W), depth (D), clad area (A_{Clad}), melted substrate area (A_{Melt}), and wetting angle (α) can be easily measured. In contrast to (b), which can measure only one location of a single-track, an entire single-track's H, W, and surface roughness (SR) can also be measured via surface profilometry, as shown in (d), to determine a track's geometric consistency quantitatively.

Figs. 5 and 6. These graphs present all single-track data (irrespective of *FH* given its observed minimal effects on the single-track geometries) as functions of a few different parameters. In Fig. 5, P and V are collapsed into the P/V parameter, Linear Energy Density ($LED, J/mm$), and plotted against $\dot{m}$. The color contours highlight different single-track geometrical features. In Fig. 6, $\dot{m}$ and V are collapsed into the $\dot{m}/V$, Mass Deposition Rate ($MDR, mg/mm$) parameter, which measures the amount of mass deposited per unit length, and this is plotted against P and single-track geometrical features as color contours. Note here that combining geometrical information irrespective of *FH* in these graphs was only done because of its observed minimal influence on single-track geometries; adapting such a procedure should be done cautiously in the case of other *FH* levels, which might have more pronounced effects on single-track geometries.

Insert Para text Here

First, notice that maps showing single-track H (Figs. 5a and 6a) and A_{Clad} (Figs. 5d and 6d) are well correlated with one another, as are maps showing D (Figs. 5b and 6b) and A_{Melt} (Figs. 5e and 6e). In Fig. 5b and e, higher *LED* leads to greater D and A_{Melt}, in particular at low $\dot{m}$; also, higher *LED* and $\dot{m}$ together lead to higher H and A_{Clad} (Fig. 5a and d). These relationships between processing parameters and single-track geometries are rationalized readily as larger $\dot{m}$ results in greater power attenuation due to larger amounts of powder being blown into the laser [71], which effectively reduces D and A_{Melt} while increasing H and A_{Clad} as more material is being fed to the laser. Since the build rate is proportional to A_{Clad}, it can also be said that a combined higher *LED* and $\dot{m}$ leads to faster build rates but potentially poorer track welding (i.e., low A_{Melt}) due to power attenuation effects. This effect is perhaps seen more clearly in Fig. 6a and d, where H and A_{Clad} increase with higher coupled P and *MDR*, while D and A_{Melt} decrease linearly with increasing *MDR* (Fig. 6b and e) or decreasing P, which is expected from previous studies [41]. Interestingly, as shown in Figs. 5c and 6c, W of single tracks is predominantly influenced by P in a linear fashion; higher P increases W, as does higher *LED*. W also increases somewhat with higher *MDR*, as seen in Fig. 6c, but not with higher $\dot{m}$, as seen in Fig. 5c. Overall, Fig. 5a-e and Fig. 6a-e illustrate the capabilities of the specific DED-LB system used here to print single tracks to different geometries as a function of printing parameters; that is, if a specific track geometry is desired, it can be approximated by the information shown in Figs. 5 and 6. Similar graphs can be produced in other DED-LB systems and materials using the procedure introduced here. There are additional measurements in these figures which describe the quality of the single tracks in the interest of printing fully dense builds. The single-track *Dilution* is one of them, which is defined as [31,41,68]:

$$Dilution = A_{Melt}/(A_{Melt} + A_{Clad}). \quad (2)$$

Note that *Dilution* can also be quantified by replacing A_{Melt} with D and A_{Clad} with H [44,68], but that definition was not used here because it is less robust, owing to its locational dependence on where H and D were measured per single-track cross-section. *Dilution* ranges in value from 0 to 1 (or, equivalently, 0–100%) and is a useful parameter because it collapses two measurements into a single measurement that describes how well the track is being welded onto the substrate while also showing the proclivity for poor efficiency. For instance, a very low *Dilution* (e.g., 0.10) indicates that there is minimal welding of the melted powder into the substrate. At the same time, a value of zero describes a complete lack of fusion between track and substrate, which indicates that upon printing multi-layer builds, there will be no fusion between layers. Alternatively, a very high value (e.g., *Dilution* $>$ 0.50) indicates that excessive heating is occurring, which can lead to defects such as keyhole porosity [68], while also incurring slow build rates due to the implications of a low A_{Clad}. At *Dilution*'s maximum of 1, A_{Clad} is also zero, meaning that no track is being printed and, instead, only the substrate is being melted, perhaps due to powder evaporation [68] or mass flow issues. Fig. 5f shows that *Dilution* is higher at lower $\dot{m}$; this fact is corroborated by Fig. 6f, which indicates that *Dilution* increases with decreasing *MDR*. Essentially, these graphs display that low *MDR* or $\dot{m}$ are favorable for producing higher *Dilution* levels due to less power attenuation under these conditions. Effects of P and *LED* on *Dilution* are relatively minor in comparison with the effects of *MDR* and $\dot{m}$.

In Fig. 4c, it is evident that the spattering of partially melted powder on single track surfaces is commonly observed in DED-LB. Comparing this feature with *SR* plots in Fig. 5 g and 6 g, higher $\dot{m}$ and *MDR*s produced greater single-track *SR*. Thus, reducing $\dot{m}$ or *MDR* can help mitigate both poor *Dilution* levels, as well as the proclivity for particle spattering, which could lead to other defects [49,66,72]. Note, however,

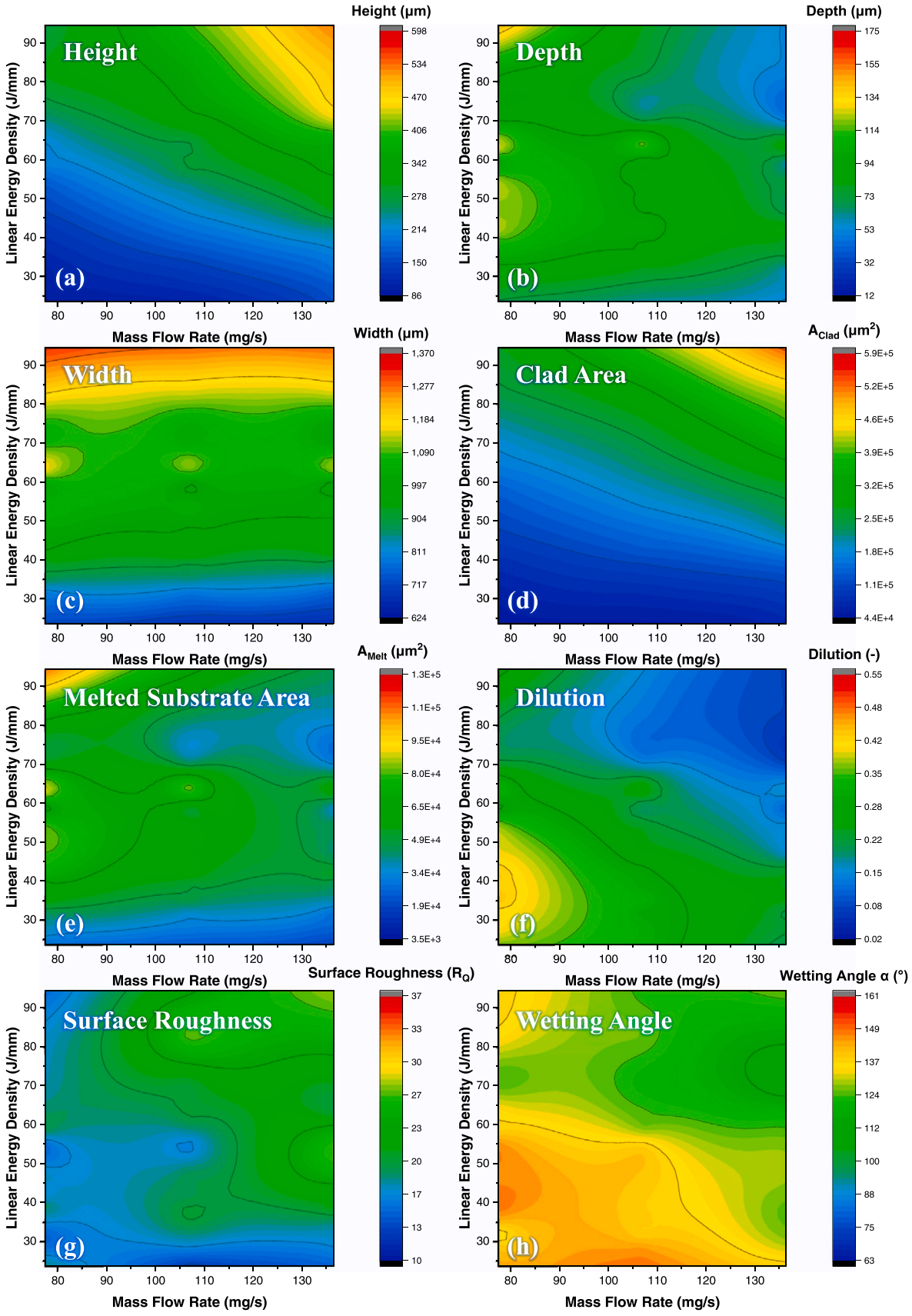

Fig. 5. Printability maps showing the effects of linear energy density (*LED*, J/mm), defined as P/V, and mass flow rate ($\dot{m}$) on various single-track geometric features: (a) height (H), (b) depth (D), (c) width (W), (d) clad area (A_{Clad}), (e) melted substrate area (A_{Melt}), (f) *Dilution*, (g) surface roughness (SR, R_q), and (h) wetting angle (α). Data from all 90 tracks was plotted here; focal height (FH) did not significantly affect single-tracks geometric measurements. Findings are summarized in Table 2.

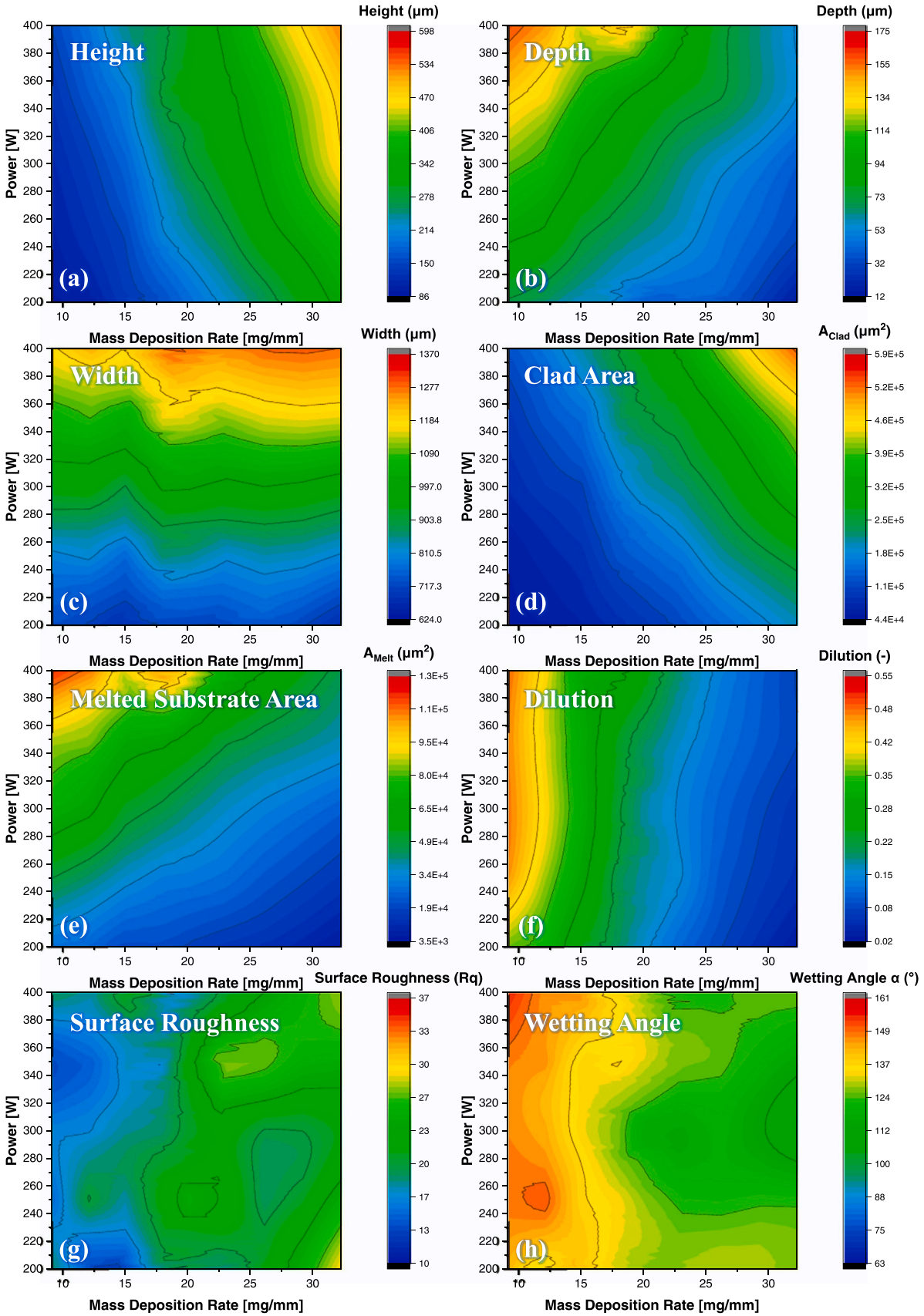

Fig. 6. Printability maps showing the effects of P and mass deposition rate (MDR, mg/mm), defined as $\dot{m}/V$, on various single-track geometric features: (a) height (H), (b) depth (D), (c) width (W), (d) clad area (A_{Clad}), (e) melted substrate area (A_{Melt}), (f) *Dilution*, (g) surface roughness (SR,R_q), and (h) wetting angle (α). Findings are summarized in Table 2.

Table 2
A qualitative summary of the correlations between single-track geometric measurements and printing parameters, correlated either positively (+) or negatively (-), or alternatively as described. These findings were extracted from the trends observed visually in Figs. 5–6.

	Summary of the Correlations between the Print Parameters and Single-Track Geometric Measurements			
	LED (J/mm) vs $\dot{m}$ (mg/s) plot		***P*** (W) vs ***MDR*** (mg/mm) plot	
	LED	$\dot{m}$	***P***	***MDR***
H (μm)	+	+	+	+
D (μm)	+ (at low $\dot{m}$)	−	+	−
W (μm)	+	No correlation	+	No correlation
A_{Clad} (μm^2)	+	+	+	+
A_{Melt} (μm^2)	+ (at low $\dot{m}$)	−	+	−
Dilution (-)	−	−	Small + correlation	−
SR (R_q)	No correlation	+	No correlation	+
α (°)	−	−	No correlation	−

that a potentially negative tradeoff from such adjustments is the slower build rates. Finally, the wetting angle α of the single tracks shown in Fig. 5h and 6 h demonstrates when compared to the *SR* and *Dilution* plots (Fig. 5f, g; Fig. 6f, g), that better *Dilution* and smoother track surfaces occur at higher α's, typically greater than 130°. Overall, the plots in Figs. 5–6 indicate that *LED*s between 30 and 50 J/mm and *MDR*s between 10 and 15 mg/mm are favorable for producing single-tracks with lower *SR*, higher α's, and higher *Dilutions*; consequently, these regions should be targeted for printing single-tracks to full density. It is worth mentioning that although previous studies by Oliveira et al. [69] and Bax et al. [24] also applied collapsed parameters and *Dilution* ranges to identify optimal laser cladding and single-track printability spaces, they did not extend these findings to printing multi-layer builds to high density. This crucial step in the DED-LB Process Optimization Framework development here is performed as described in the following sections. Table 2 summarizes the qualitative findings from Figs. 5–6.

While the qualitative visual trends established in Table 2 from Figs. 5–6 are enlightening, a more concrete statistical analysis was also conducted to quantitatively establish such trends among the different printing parameters and single-track geometries. Here, the effects of the various print parameters on single track geometric measurements were assessed by a statistical model to capture the relationship between inputs and output. This model is given by Eq. 3:

$$y = \beta_0 + \beta_1 x_1 + \beta_2 x_2 + \beta_3 x_3 + \beta_4 x_1 x_2 + \beta_5 x_2 x_3 + \beta_6 x_1 x_3 + \epsilon \quad (3)$$

where β_0 is the intercept, β_i is the coefficient, x_i is the factor level of variable i, y is the quantity of interest (QoI), and ϵ stands for random error. Before the modeling, x_i and y were transformed, such that x_i, $y \in (0, 1)$. To estimate the coefficients of this model, least squares estimation was adopted. Tables 3 and 4 show the coefficients of 8 QoIs [y] regarding various sets of factors: [x_1 = *LED*, $x_2 = \dot{m}$, x_3 = *FH*] and [x_1 = *P*, x_2 = *MDR*, x_3 = *FH*], respectively. In general, the sign of β_i shows its correlation effect with a given factor level variable. For example, if $\beta_1 = +0.2$, it means that x_1 has a positive correlation with y, or if $\beta_2 = -0.01$, it means that x_2 has a negative correlation with y, and such a correlation is also weak since its absolute value is quite small. Here, β_4, β_5, and β_6 are the correlation coefficients for the interactions of multiple factors. When their values are small, interactions of multiple factors have less of an influence on the QoIs, and vice versa.

Coefficients in Tables 3 and 4 are generally consistent with qualitative trends established visually from Figs. 5–6 and included in Table 2. The table also shows that *FH* had very minimal effects on single-track geometries. Absolute values of *FH* coefficients were mostly very small (≤ 0.05), however, for instance for *SR*, *FH* seems more significant than $\dot{m}$. Yet, as spattered particles were not included in the calculations of single-track geometries, the influence of *FH* on single track geometries was minimized. The strongest interaction terms observed were *LED* × $\dot{m}$ and *P* × *MDR*, as expected from Figs. 5–6.

3.2. Deriving hatch spacing and layer thickness criteria to maximize density

In the previous section, the relationships between *P*, *V*, and $\dot{m}$ printing parameters and single-track characteristics have been estab-

Table 3
Statistical model coefficients for single-track features as a function of individual factors, *LED*, $\dot{m}$, and *FH*, and their interactions.

	y = ***H***	y = ***D***	y = ***W***	$y = A_{Clad}$	$y = A_{Melt}$	y = ***Dil***	y = ***SR***	$y = \alpha$
β_0	-0.04	0.54	0.20	-0.03	0.37	0.81	0.18	0.83
β_1(***LED***)	0.52	0.15	0.75	0.48	0.38	-0.43	0.13	-0.28
$\beta_2(\dot{m})$	0.17	-0.19	-0.09	0.04	-0.14	-0.42	0.06	-0.24
β_3(***FH***)	0.04	-0.02	-0.02	0.03	-0.03	-0.03	0.15	-0.06
β_4(***LED*** × $\dot{m}$)	0.35	-0.30	0.00	0.43	-0.31	0.04	0.37	-0.09
$\beta_5(\dot{m} \times$ ***FH***)	-0.05	0.07	0.05	-0.02	0.08	0.08	-0.04	0.12
β_6(***LED*** × ***FH***)	-0.12	0.09	0.02	-0.11	0.07	0.06	-0.18	0.16

Table 4
Statistical model coefficients for single-track features (y) as a function of individual factors, *P*, *MDR*, and *FH*, and their interactions.

	y = ***H***	y = ***D***	y = ***W***	$y = A_{Clad}$	$y = A_{Melt}$	y = ***Dil***	y = ***SR***	$y = \alpha$
β_0	-0.06	0.38	0.06	-0.05	0.18	0.68	0.09	0.75
β_1(***P***)	0.20	0.54	0.73	0.18	0.70	0.11	0.20	0.10
β_2(***MDR***)	0.61	-0.35	-0.05	0.32	-0.20	-0.73	0.37	-0.43
β_3(***FH***)	0.05	0.00	0.01	0.04	-0.01	-0.02	0.20	-0.04
β_4(***P*** × ***MDR***)	0.20	-0.35	0.17	0.47	-0.39	-0.06	-0.02	-0.21
β_5(***MDR*** × ***FH***)	-0.08	0.03	0.06	-0.06	0.03	0.02	0.02	0.21
β_6(***P*** × ***FH***)	-0.10	0.10	-0.03	-0.08	0.09	0.11	-0.29	0.04

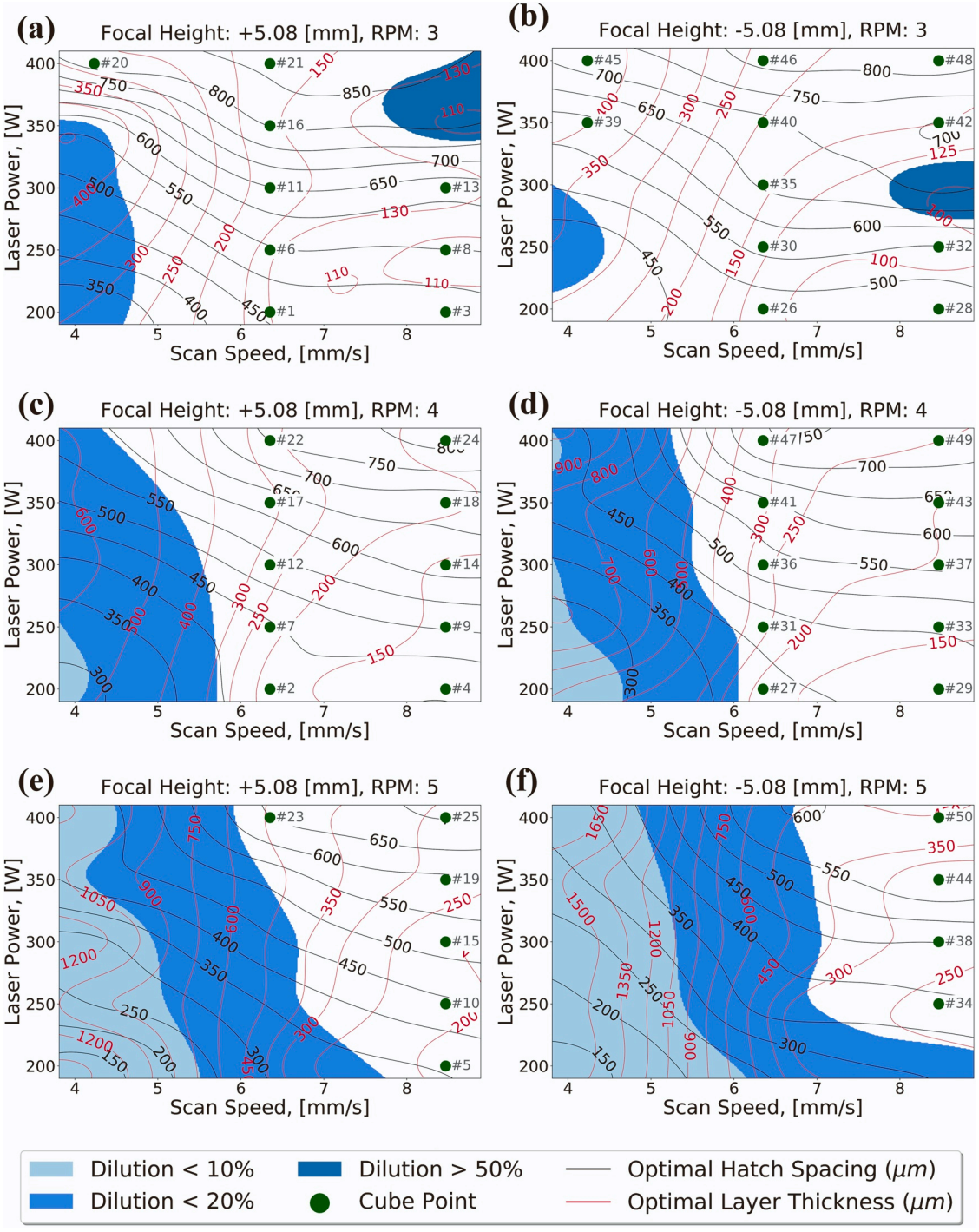

Fig. 7. Printability maps for DED-LB of AF9628 steel constructed using single-track experiments. (a), (c), and (e) present three slices of the P-V space, at 3, 4, and 5 RPMs, respectively, for the diffuse laser focal height (FH) of + 5.08 mm (i.e., the laser focal plane is located 5.08 mm above the substrate surface). (b), (d), and (f) display the same for the non-diffuse FH of −5.08 mm (i.e., the focal plane is located 5.08 mm below the substrate surface). The white region shows the optimal printing area (20 % < Dilution < 50 %) to eliminate printing induced porosity, where contours capture optimal hatch spacing (black) and optimal layer thickness (red) settings. Printing of 50 cubes was attempted, as shown via the green dots; cubes #1–25 were successfully printed. Cubes #26–50 (b, d, and f) exhibited excessive spattering and could not be completed. As FH did not affect single-track geometry, both sets of printability maps look similar.

lished (in Figs. 5–6 and Tables 2–4) by constructing maps and models showing the effects of collapsed parameters, *LED* or *MDR*, on single-track geometric features. As a result, the general processing parameter combinations that favor desirable single-track characteristics have been identified. However, caution is warranted: collapsing parameters can result in lost information. For instance, very different values of *P* and *V* or *V* and $\dot{m}$ can result in identical values of *LED* or *MDR*, respectively. Therefore, the collapsed parameters can obscure the effects of extreme values of *P*, *V*, and $\dot{m}$. Consequently, in addition to the descriptive contour plots of *LED* vs. $\dot{m}$ and *P* vs. *MDR* in Figs. 5–6, it is also instructive to analyze the *P* vs. *V* plots as a function of $\dot{m}$ to correctly utilize the optimal printability space and present some of the single-track geometric features in these plots. This is exemplified in Fig. 7, where (a), (c), and (e) show the printability maps for 3, 4, and 5 *RPMs* (i.

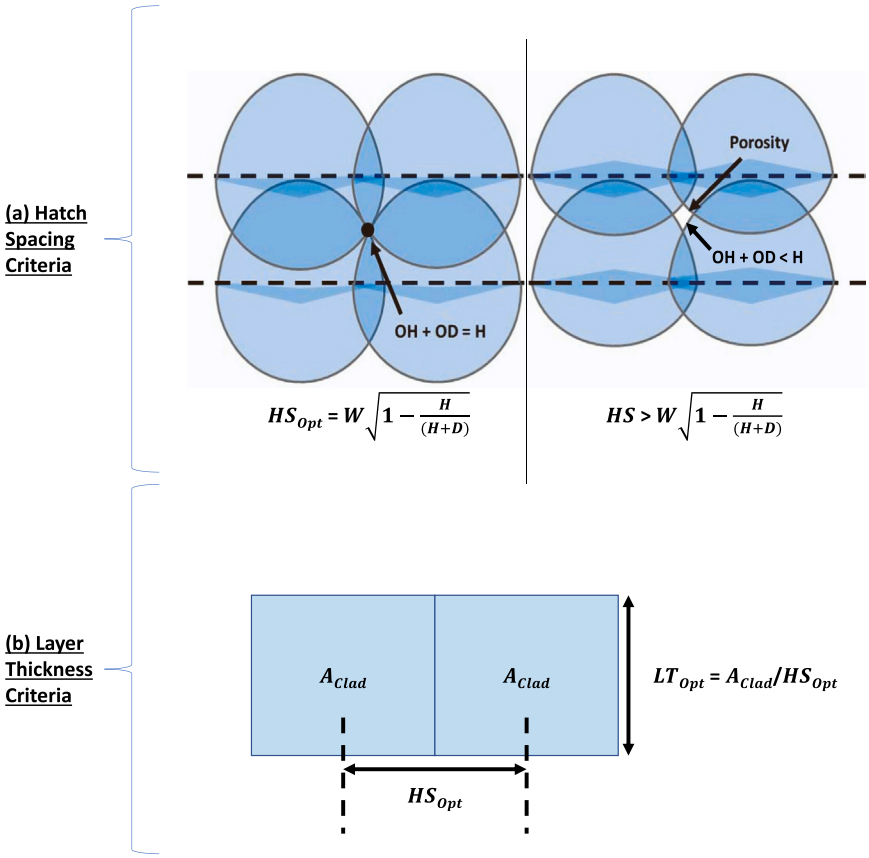

Fig. 8. The schematic illustrating the concepts behind the criteria for (a) optimal Hatch Spacing (HS_{Opt}) and (b) optimal Layer Thickness (LT_{Opt}) values when printing bulk samples in DED-LB. In (a), HS_{Opt} is calculated to ensure no interlayer and inter-track porosity exists, by setting the sum of the Overlap Height (OH) and Overlap Depth (OD) equal to the single-track height (H). (a) was modified slightly from [8], where the HS criterion was constructed for L-PBF. In (b), LT_{Opt} assumes the deposited clad geometry as a rectangle with no overlap or a gap between the tracks, an assumption made possible by following the HS_{Opt} settings. Thus, the actual LT can be set equal to the deposited area A_{Clad} divided by the HS_{Opt}. LT_{Opt} is thereby set to adjust according to the changes in HS_{Opt}.

e., $\dot{m}$ of 77.6, 107.1, and 136.6 mg/s) at a FH of + 5.08 mm, and (b), (d), and (f) present the same for a FH of −5.08 mm.

As mentioned in the previous section, notice here that the plots show consistency between the two FHs, indicating the minimal effects of FHs on single track geometries. Optimal printability regions are shown in white, where varying *Dilution* zones (less than 20% and more than 50%) are shown as well in different shades of blue. This optimal *Dilution* range of 20% to 50% was chosen because *Dilution* too close to 0 results in lack of fusion between layers, leading to low density and poor mechanical properties. Also, if *Dilution* is too high, then built rate becomes low and inefficient. A balance must therefore be struck between printing fully dense parts and printing efficiently. Thus, a 20–50% optimal *Dilution* range is conservative, allowing for the production of fully dense components with reasonable efficiency and volume build rates.

To promote full density by preventing the systematic formation of porosity, HS and LT values must be appropriately selected [40]. HS that is too wide or too narrow can, respectively, result in either cavities between tracks or excessive overlap, which can, in turn, lead to rough, graded build heights or porosity between successive tracks [40]. Suboptimal LT values can cause inaccurate final build heights, variable FHs, interlayer porosity, inconsistent mass delivery due to deviations from the ideal nozzle displacement to the print surfaces, and powder oxidation, evaporation, and spattering due to insufficient LTs that yield excessively high energy densities to the melt pool. With this in mind, the optimal settings for printing single tracks with favorable *Dilution* ranges (taken as 20–50% in this study) may not remain optimal if the LT is set incorrectly, potentially resulting in variable working distances and inaccurate actual layer heights. Additionally, suboptimal HS can cause inconsistent layer thicknesses due to interlayer porosity or excessive overlap.

Given that HS can affect the effective LT, coupled HS and LT criteria are needed to print bulk samples to full density. The geometry of single tracks can be utilized to derive the appropriate relationships. Regarding HS, as shown for L-PBF [8,10,73,74], an optimal hatch spacing criterion can be derived from single-track dimensions, W, H, and D. As illustrated in Fig. 8a, with single-track cross-sections modeled as parabolas, HS must be set to ensure that the overlap height (OH) plus the overlap depth (OD) of adjacent tracks is equal to H. This will lead to complete melting during the deposition of a second layer and fill the gaps between adjacent tracks. If the $OH+OD$ is greater than H, a greater fusion occurs between tracks. However, this can lead to uneven layers, especially towards the limit of near zero HS, where in DED-LB, unlike L-PBF, tracks located too close together build upwards progressively given the constant mass flow, forming an uneven surface [51,75]. This, in turn, destabilizes the mass flow from its optimal focal point with respect to the laser profile [25]. In contrast, if $OH+OD$ is less than H, a lack of fusion would occur between adjacent tracks, similar to L-PBF. The optimal hatch spacing (HS_{opt}) for DED-LB is thus defined as (Fig. 8a):

$$\mathrm{HS}_{opt}(\mu m) = W\sqrt{1-\frac{H}{(H+D)}} \tag{4}$$

as a function of single-track W, H, and D. Since HS affects the effective layer height in DED-LB, a criterion defining optimal LT (LT_{opt}) can be derived by idealizing the cross-sectional geometry deposited per track (i.e., A_{Clad}) as a rectangle, without any overlap or gap between single-tracks (see Fig. 8b), by setting the HS to the optimal value (Eq. 3). LT_{Opt} is, therefore, calculated using the Eq. 5:

$$LT_{Opt}(\mu m) = A_{Clad}/HS_{Opt} \tag{5}$$

where it is evident that LT_{Opt} is inversely proportional to HS_{Opt}. A larger HS_{Opt} will therefore result in lower layer heights, and vice versa; this makes sense intuitively, as increasing HS will result in lower layer heights due to lack of buildup between tracks and lower mass deposited per layer.

Table 5
Table of the relevant processing parameters used for the 25 AF9628 cubes printed at a focal height (FH) of + 5.08 mm. Cubes were not set to have the same target heights, but to exceed a minimal height of 4.45 mm each.

Cube Number	P (W)	V (mm/s)	Mass Flow Rate (mg/s)	Hatch Spacing (μm)	Layer Thickness (μm)	Focal Height (mm)	Center Purge Ar Flow (L/min)	Carry Gas Nozzle Ar Flow (L/min)	Printed for Tension? (Yes/No)
1	200	6.35	77.6	451	120	5.08	28	3	N
2	200	6.35	107.1	419	194	5.08	28	3	N
3	200	8.47	77.6	468	124	5.08	28	3	N
4	200	8.47	107.1	369	172	5.08	28	3	N
5	200	8.47	136.6	313	204	5.08	28	3	N
6	250	6.35	77.6	567	144	5.08	28	3	N
7	250	6.35	107.1	428	256	5.08	28	3	N
8	250	8.47	77.6	524	111	5.08	28	3	N
9	250	8.47	107.1	522	146	5.08	28	3	N
10	250	8.47	136.6	426	224	5.08	28	3	N
11	300	6.35	77.6	713	137	5.08	28	3	Y
12	300	6.35	107.1	522	279	5.08	28	3	N
13	300	8.47	77.6	617	146	5.08	28	3	N
14	300	8.47	107.1	590	162	5.08	28	3	Y
15	300	8.47	136.6	544	190	5.08	28	3	N
16	350	6.35	77.6	793	169	5.08	28	3	Y
17	350	6.35	107.1	621	313	5.08	28	3	N
18	350	8.47	107.1	635	214	5.08	28	3	N
19	350	8.47	136.6	542	308	5.08	28	3	N
20	400	4.23	77.6	802	295	5.08	28	3	N
21	400	6.35	77.6	871	165	5.08	28	3	Y
22	400	6.35	107.1	751	267	5.08	28	3	N
23	400	6.35	136.6	638	443	5.08	28	3	N
24	400	8.47	107.1	805	190	5.08	28	3	Y
25	400	8.47	136.6	693	313	5.08	28	3	N

Overall, Eq. 4 works to prevent progressive overbuilding while maintaining fusion between single tracks and layers, and it works in conjunction with Eq. 5 to set a *LT* that identifies the optimal amount of z-displacement that prevents changes in *FH* or mass flow in between layers. Concurrently, one can estimate that a single track's *Dilution* can remain consistent in between layers. Without criteria for layer thickness such as Eq. 5, geometrical accuracy is poorly controlled, as the mass captured by the laser for each layer varies with working distance [76]. Altogether the following three criteria have been established as guidelines for the DED-LB Process Optimization Framework:

I. *Dilution* should be between 20% and 50%,
II. *HS* should be set according to Eq. 4, and
III. *LT* should be set according to Eq. 5.

Application of these three criteria should enable printing bulk samples to full density. A validation for the present DED-LB Process Optimization Framework is explored in the next section.

Fig. 7 presents two sets of contours, HS_{Opt} (black) and LT_{Opt} (red), completing the printability maps for the AF9628 steel in the Optomec LENS MR-7. Similar maps can be produced for any DED-LB system following the DED-LB Process Optimization Framework introduced here. As such, one can pick any *P*, *V*, and $\dot{m}$ (or *RPM*, equivalently) parameter combination within these maps to determine if they would be sufficient to print fully dense bulk samples by assessing its projected *Dilution*. If the *Dilution* is favorable (i.e., between 20% and 50%), one should be able to utilize the HS_{Opt} and LT_{Opt} contours to set the appropriate *HS* and *LT* that promote maximal density in bulk prints.

4. Applying the DED-LB process optimization framework to print bulk samples

4.1. Density measurements and sample height accuracy

The DED-LB Process Optimization Framework introduced in Section 3 can be deemed successful if the printed bulk cube densities resemble

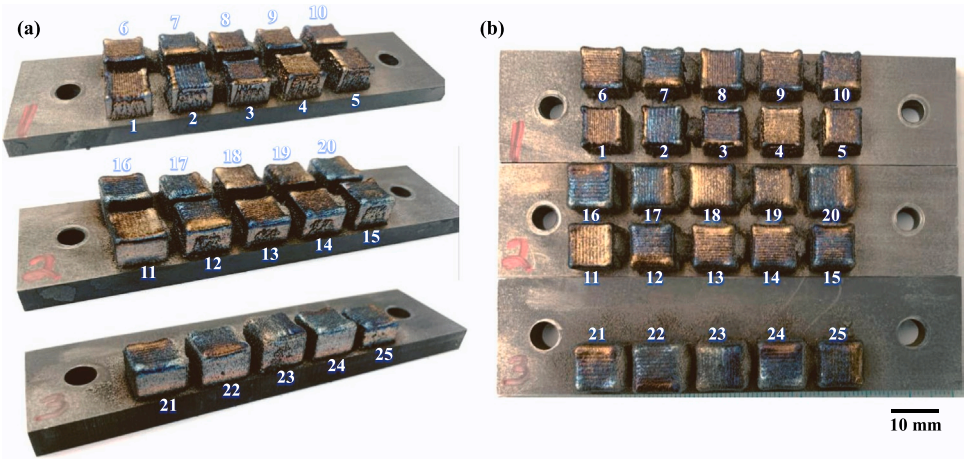

Fig. 9. (a) auxiliary and (b) top views of AF9628 cubes #1–25 printed via the DED-LB Process Optimization Framework according to the parameters listed in Table 5.

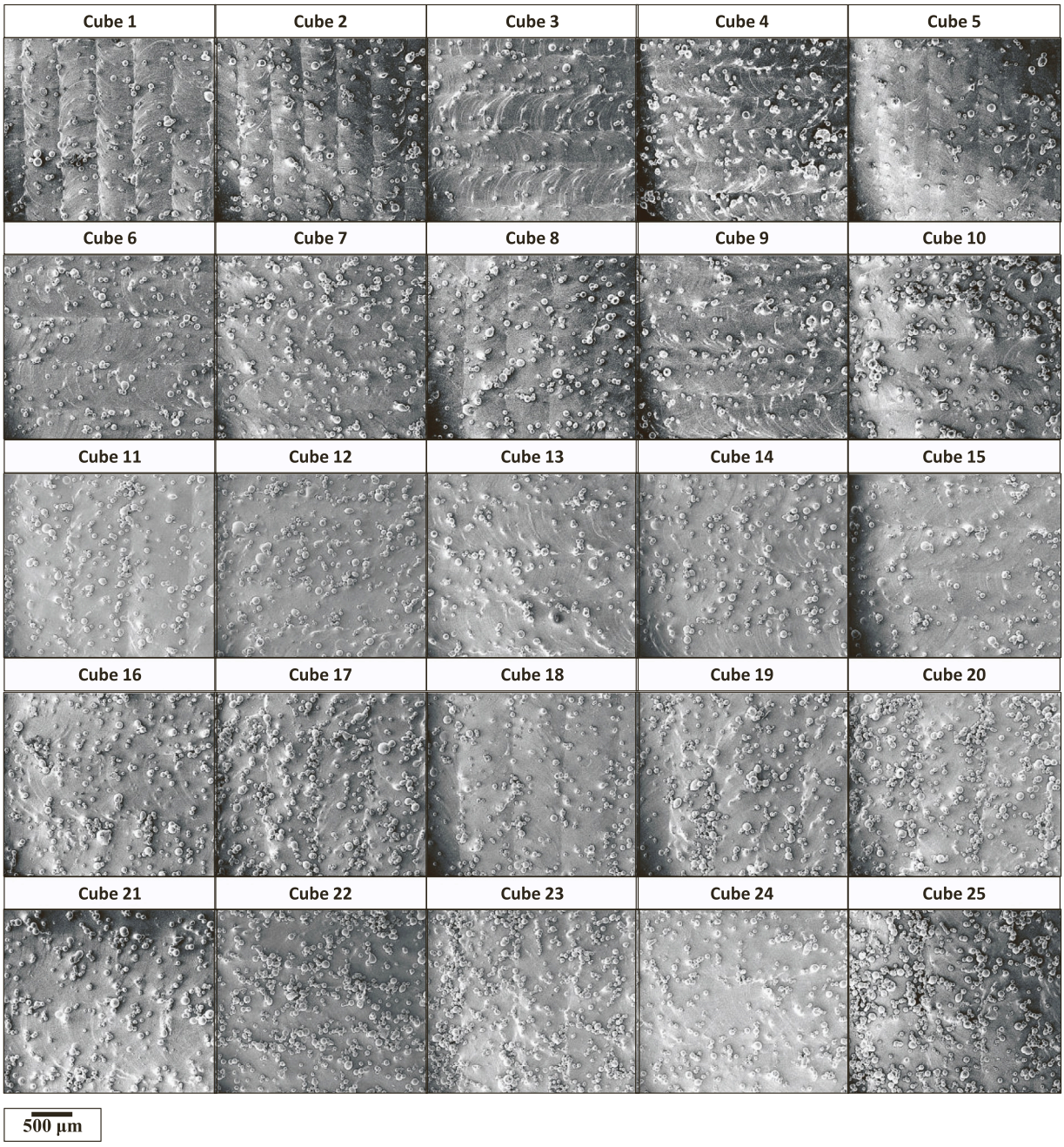

Fig. 10. Scanning electron (SE) microscopy images of the AF9628 steel surfaces for the cubes #1 through #25 (Fig. 9 and Table 5) printed utilizing the DED-LB Process Optimization Framework introduced here at the *FH* of + 5.08 mm. The tracks can be resolved in the images and show that the HS_{Opt} criterion works well in printing adjacent tracks without inter-track porosity. A number of unmolten particles is observable on the sample surfaces, especially at higher mass flow rates ($\dot{m}$).

the densities of the wrought alloy. Additionally, the printed cube heights should be consistent with the predictions from the LT_{Opt} criterion to confirm that the laser *FH* and the mass flow dynamics remain consistent throughout the print. Finally, the most representative and perhaps most accurate measure of full density in a printed sample is tensile strength and ductility comparable to those from the wrought alloy. With this in mind, to validate the present framework, specific parameter combinations were chosen (indicated by the green circles, which are labeled from #1–50, in Fig. 7) for printing 50 cubes in total, 25 per *FH*. All the cubes were printed following the criteria I, II, and III outlined in Section 3.2.

Printing cubes #1–25 at a *FH* of + 5.08 mm was completed without any issues. However, when printing cubes #26–50, samples began to form excessive spatters during the printing. The two sets of printability maps at different *FHs* (Fig. 7) look quite similar; nevertheless, the detrimental effect of a non-diffuse *FH*, −5.08 mm, became apparent only during printing cubes, perhaps due to greater heat buildup. At the melt pool, it is likely that non-diffuse FHs apply more heterogenous laser power intensities with greater energy spikes in the laser profiles (example laser profiles can be found in Ref. [25]) in comparison to diffuse FHs and are therefore more sensitive to minor height fluctuations upon the building of multi-layered samples. Overall, it was impossible to complete cubes #26–50 at the −5.08 mm *FH*, and it is recommended, from these findings and others [57,77], that one must utilize diffuse *FHs* when printing via DED-LB. The corresponding print parameters for the successfully printed cubes #1 through #25 are listed in Table 5, and the printed cubes are shown in Fig. 9, numbered according to their

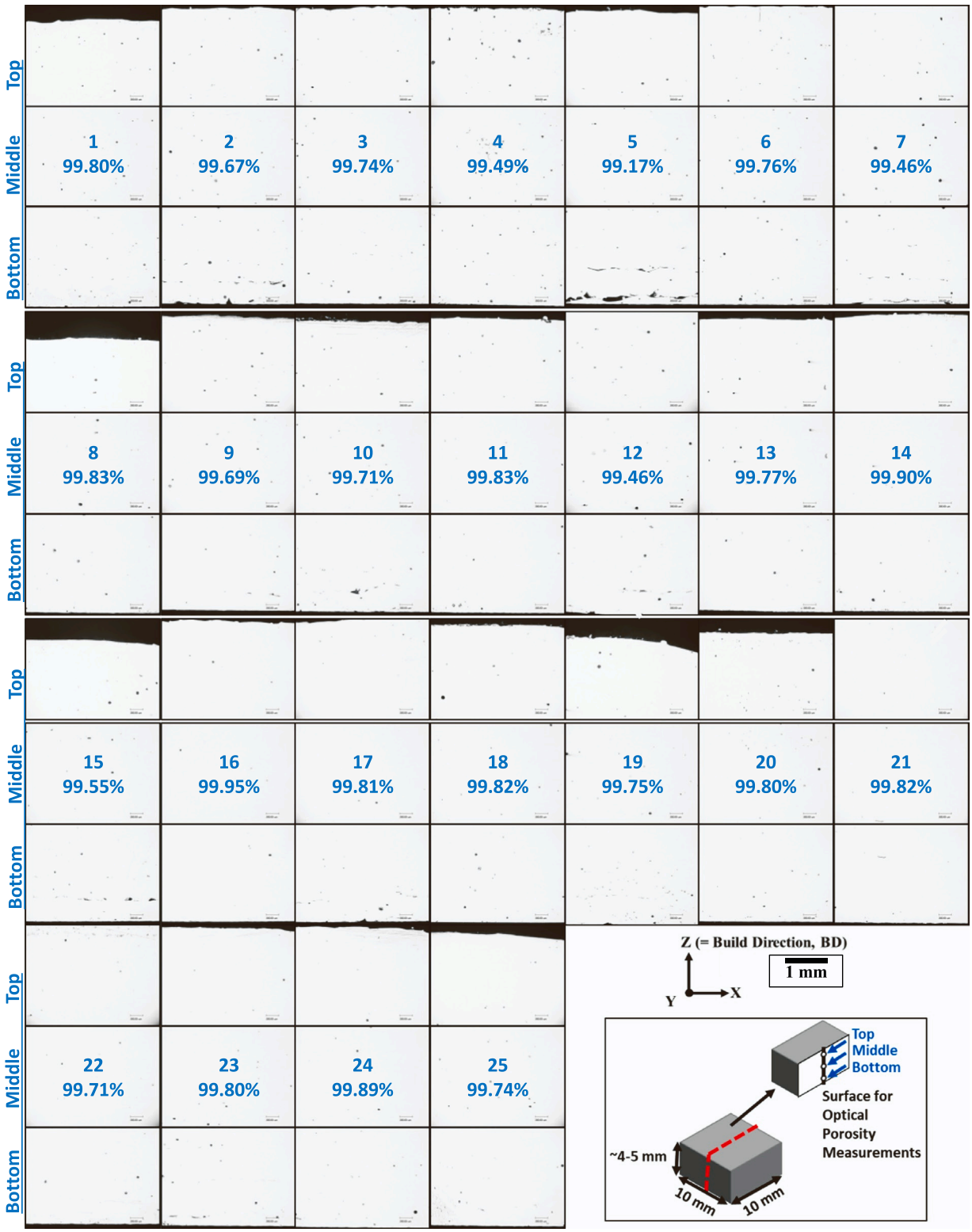

Fig. 11. Optical microscopy (OM) images of the inside middle surface, with a schematic inset showing image locations, for the AF9628 steel cubes #1 through #25 printed at the FH of + 5.08 mm to near full (>99 %) density. The density values shown for each case were calculated by subtracting the area fraction of the porosity in three images shown from 100 %. The bottom, middle, and top regions are shown for each cube. The cube bottoms sometimes had porosity issues (e.g., cube 5), attributable to faster cooling rates near the substrate surface. The images demonstrate that applying the three printing criteria (*Dilution*, HS_{Opt}, LT_{Opt}) of the presented DED-LB Process Optimization Framework successfully produced near fully dense (>99 %) builds.

parameter set.

Next, the printed cube surfaces were characterized, as shown in Fig. 10, which indicates the success or failure of the selected HS_{Opt} and LT_{Opt} values. From Fig. 10, it is apparent that inter-track porosity appears minimal, as gaps are not obvious between adjacent tracks, indicating the success of the selected criteria in Eqs. 4 and 5. Next, the densities of the cubes were measured by two standard methods: the Archimedes method and porosity measurements using optical

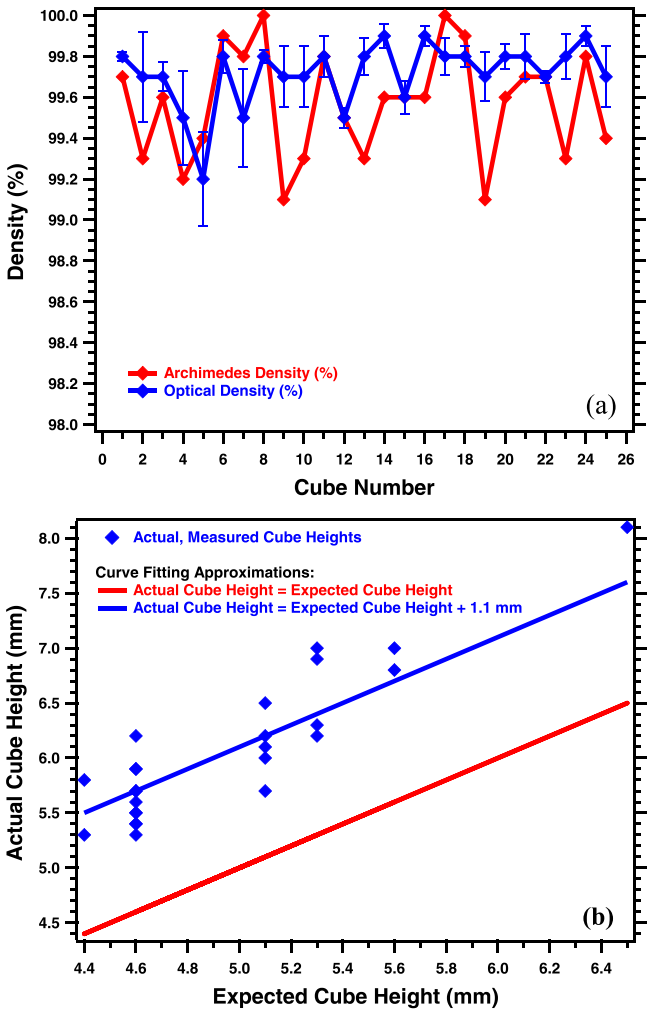

Fig. 12. Figures displaying (a) optical and Archimedes method densities and (b) actual versus expected target cube heights of AF9628 steel cubes #1–25 (Fig. 7a,c,e and Table 5). On average, cubes were 1.1 mm taller than the target heights, yet consistently and predictably so, as seen from the blue line in (b).

microscopy. Archimedes density measurements were indicative of the overall cube density, whereas optical porosity measurements were useful for verification, via visual analysis, of the Archimedes density measurements. As shown in Fig. 11, the optical density of all cubes #1–25 exceeded 99 %, which is excellent for the DED-LB method and is tangible evidence of the success of the DED-LB framework methodology. Note, however, that some porosity is still present in Fig. 11; of which two types were evident. First, a lack of fusion existed for a few cubes, #2, #5, #7, #10, and #12, at the cube bottoms. This defect is probably related to a larger heat flux during the beginning of a print [78], as the substrate was unheated, and the initial few layers were exposed to less thermal buildup than most of the upper layers. Nevertheless, it is desirable to eliminate this defect, and it is plausible that substrate pre-heating could mitigate it.

In addition to the lack of fusion defects at the bottoms of the cubes, spherical pores were also evident for the bottom, middle, and top areas of all cubes printed. These pores are arranged randomly, indicating that they were not symptomatic of failures in the *LT* or *HS* criteria, which should manifest as systematic porosity. Thus, these spherical pores should be a consequence of random gas entrapment that may come from the entrapped gas porosity in the initial powder particles or can occur during printing due to randomness in mass flow, powder distribution, and heat transfer events [25,78–80]. Such pores have been reported to occur, for example, from localized slower cooling rates and greater heat buildup [78], factors which fluctuate at times during DED-LB due to slight deviations in mass flow rates, focal height, and other parameters during building. Several methods to eliminate these pores are available – for instance, utilizing a different nozzle design (such as a coaxial nozzle or a nozzle with a lower angle [76]) can provide a more uniform powder supply to the laser resulting in more homogenized and even heat transfer. Alternatively, a rescanning pass without powder could also melt material into these pores, fusing them to the surrounding metal [72,81]. The success of such techniques has not been investigated further herein for brevity but would be worth investigating in a future study.

The Archimedes (red) and optical density (blue) measurements are compared for cubes #1–25 in Fig. 12a. Overall, the cubes' densities were all excellent, above 99 %, clearly demonstrating the effectiveness of the DED-LB Process Optimization Framework in producing fully dense parts across an array of printing parameters. When observing the two measurements in Fig. 12a, one can see that a perfect correlation in the trends between the two density measurements cannot be established, indicating some inherent error in both measurements. This observation is explainable from the fact that Archimedes density measures the bulk density while optical density only measures from various slices of the sample.

Fig. 12b shows the measured cube heights (blue) versus the expected cube heights (red line). Here, the expected cube heights were calculated as the product of the *LT* and the number of layers. The actual cube heights were about 1–2 mm above the expected ones. However, their trend is overall fairly linear, described by the following equation:

$$ActualCubeHeight(mm) = ExpectedCubeHeight(mm) + 1.1mm \quad (6)$$

as shown by the blue line. Here, a constant offset of 1.1 mm from the perfect 1:1 fit shown by the red line gives accurate build heights to ± 0.5 mm. Such an offset may occur for a variety of reasons, such as changes in heat buildup, powder flow, and *SR* from the initial to the final layers. In general, geometrical accuracy in deposition based AM is challenging [82], but Fig. 12b indicates that final build heights are predictable for DED-LB when applying the LT_{Opt} criterion (Eq. 5 in Section 3.2) to a given parameter set. Further improvements should be possible with feedback control methods [65].

4.2. Mechanical properties of tensile samples

Five cube parameters corresponding to cubes #11, 14, 16, 21, and 24 were selected for the printing of tensile samples, as these possessed the highest optical densities, with Archimedes densities measuring above 99 %. As neither method for measuring density provides information on the shape and distribution of defects throughout the bulk part, tension test responses were a more comprehensive method for measuring the success of the framework. Table 5 shows these cube print parameters in detail, and Fig. 13 captures their engineering stress vs. engineering strain curves. Overall, Fig. 13a-e shows three tensile curves for each parameter combination, where general consistency in strength and ductility is apparent for each.

The overall mechanical properties for each condition are summarized in Table 6. From Table 6 and Fig. 13f, a comparison among all 5 tensile sample parameter sets shows general consistency in properties. Therefore, it appears that print parameters (i.e., *P*, *V*, $\dot{m}$, HS_{Opt}, and LT_{Opt}) had minimal effects on mechanical properties; the framework worked consistently well for all parameter combinations shown in Table 5 for cubes #11, 14, 16, 21, and 24. The repeatability and consistency in mechanical properties indicate that following the DED-LB Process Optimization Framework ensures printing nearly defect-free parts with repeatable mechanical performance. Indeed, this is a strength of this study, as consistent mechanical properties via DED-LB is often very difficult to achieve due to the many involved processing parameters [32].

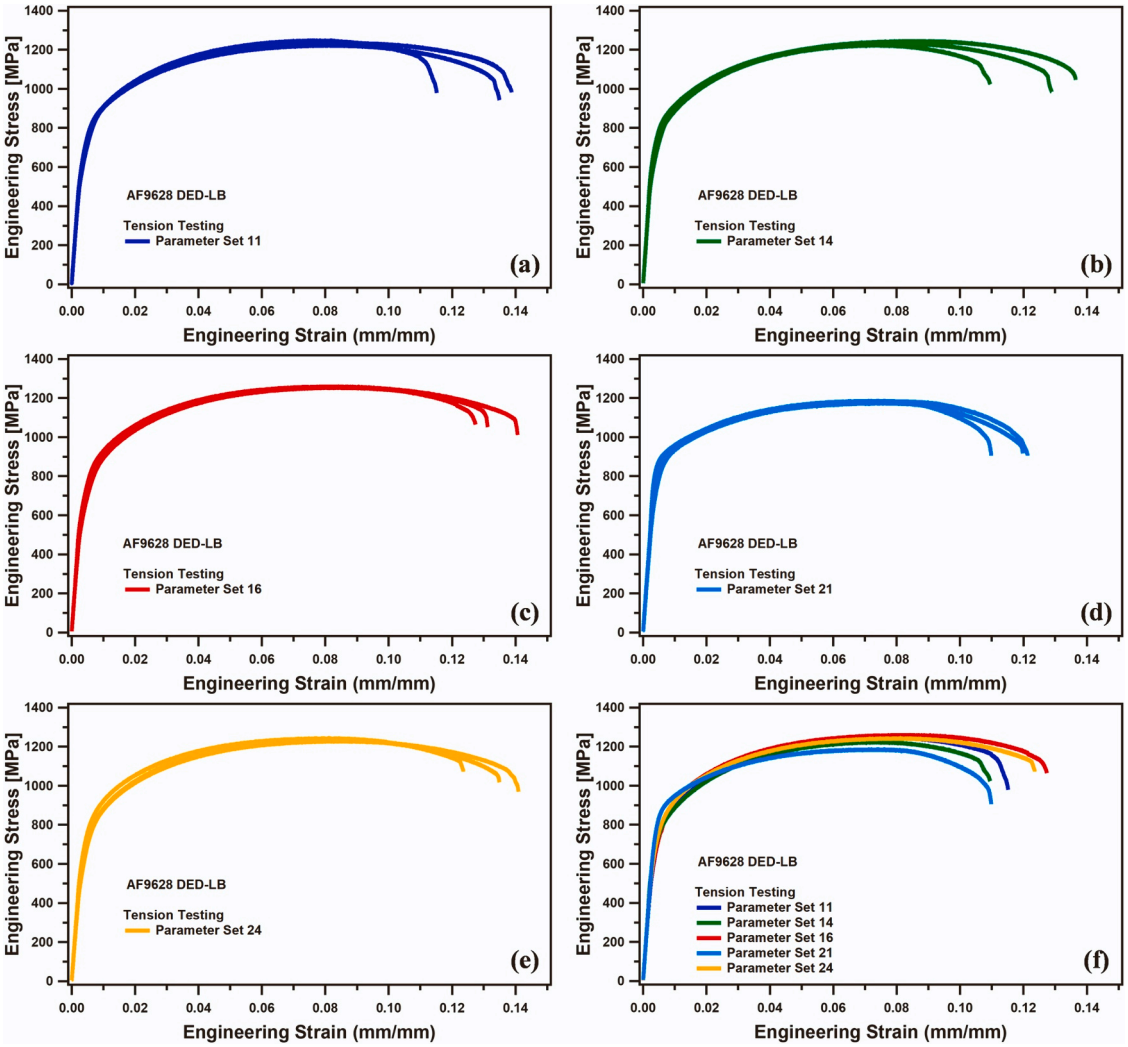

Fig. 13. Engineering stress versus strain curves for the five tension blocks printed according to the parameter settings shown (see Table 5). Three replicates were tested per block, showing general consistency per block, as shown in (a) – (e), with σ_{Yield} around 800 MPa, σ_{UTS} around 1200 MPa, and ε_f around 12–14 %. Overall, responses across all 5 blocks are consistent (f). Mechanical properties are summarized in Table 6.

4.3. Microstructural analyses of DED-LB printed tensile samples

Corroborating evidence for the consistency across print parameter sets was also found in the microstructural analyses. EBSD was taken at the gage section for tension samples prior testing, as shown by the blue rectangle in Fig. 14. Corresponding EBSD maps in Fig. 15 show martensite lath sizes appear roughly similar across samples, and prior austenite grains were also evaluated, as shown in Fig. 16, from the same images. A 15–48° grain misorientation range was used to reveal the prior austenite grain boundaries. Notice that the images in Fig. 16 also display the phase fraction maps, where a phase fraction exceeding 98.5 % belonged to BCT martensite in each sample.

Overall, prior austenite grains (PAGs) appear elongated along the build direction, which is typically expected [8,60,74,83,84]. In Fig. 17a and b, the martensite lath and PAG equivalent diameters were calculated and plotted for each tension sample. Overall, these images demonstrate general consistency across martensite lath sizes and prior austenite grain sizes, as expected given the similar mechanical properties shown in Fig. 13. Also, when analyzing the texture from the inverse pole figure insets per each map in Fig. 15, weak textures were present for all conditions along the tensile direction (TD); most samples did not exhibit pronounced (001) textures along the build direction (BD), which is typical for additively manufactured steels [83]. It is plausible that the weak texturing was a consequence of the slower cooling rates in DED-LB versus L-PBF [84]. Although Parameter Set 16 showed (001) texturing along the BD, the tensile response was fairly similar to the other samples where no such texturing occurred (Fig. 13), indicating that texture did not have a significant effect on the mechanical properties.

The effects of the process parameters, introduced in the present DED-LB Process Optimization Framework, on the microstructure and mechanical properties of the tested samples were negligible. Overall, the results demonstrate that near full density (>99 %) and consistent mechanical properties and microstructures were achievable for the various combination of process parameters. This indicates that following the DED-LB Process Optimization Framework can yield parts with similar mechanical performance across different sets of print parameters for this AHSS.

5. Discussion of the results

5.1. Comparisons of AF9628 martensitic steel properties across different thermomechanical processing methods

In assessing the overall success of the DED-LB Process Optimization Framework for printing the martensitic AF9628 AHSS, it is instructive to compare the mechanical properties and target alloy compositional ac-

Table 6
Average and standard deviations of measured mechanical properties, showing yield strength (σ_{Yield}), ultimate tensile strength (σ_{UTS}), and elongation to failure (ε_f) under tension for the AF9628 Martensitic Steel under different thermo-mechanical processing conditions. The DED-LB tension samples were printed using 5 different process parameters sets (please refer to Table 5 for the parameters).

AF9628 Condition	σ_{Yield} (GPa)	σ_{UTS} (GPa)	ε_f (%)
Wrought - Baseline	1.38 ± 0.00	1.75 ± 0.04	7.40 ± 0.56
DED As-Printed			
Parameter Set 11	0.76 ± 0.04	1.24 ± 0.01	12.30 ± 1.31
Parameter Set 14	0.77 ± 0.05	1.23 ± 0.01	12.83 ± 0.55
Parameter Set 16	0.75 ± 0.05	1.26 ± 0.00	12.83 ± 0.71
Parameter Set 21	0.90 ± 0.02	1.18 ± 0.01	11.30 ± 0.70
Parameter Set 24	0.75 ± 0.04	1.24 ± 0.01	12.87 ± 0.91
L-PBF As-Printed + Heat Treated (HT)			
As Printed [8]	1.08 ± 0.00	1.43 ± 0.00	9.79 ± 0.14
As Printed + HT1 [10]	1.21 ± 0.04	1.54 ± 0.00	7.15 ± 0.13
As Printed + HT2 [10]	1.40 ± 0.01	1.66 ± 0.01	5.37 ± 1.00
As Printed + HT3 [10]	1.31 ± 0.06	1.66 ± 1.1	7.63 ± 0.04

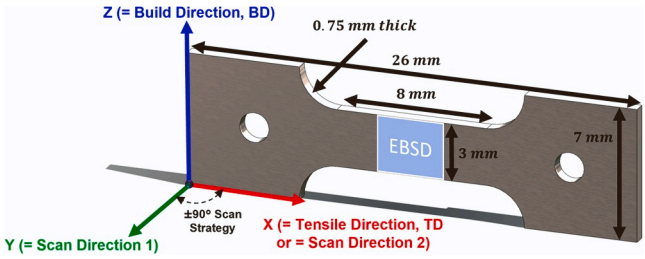

Fig. 14. Schematic illustrating the tensile samples relative to the DED-LB print directions and collected EBSD maps.

curacy for this material across different processing methods, from the wrought Baseline condition to the as-printed L-PBF and DED-LB conditions. Such comparisons are provided in Fig. 18 and Table 6, where it is evident that the wrought AF9628 Baseline condition exhibits the best σ_{Yield} and σ_{UTS} levels, followed by L-PBF printed AF9628 and, finally, by DED-LB printed AF9628. Likewise, as expected, the ε_f increases in the same order, coinciding with the reduction in σ_{Yield} and σ_{UTS}.

In general, in steels strengthening can be achieved via the four mechanisms of solid solution strengthening, dislocation strengthening, grain boundary strengthening, and precipitation strengthening. Strength reduction is expected to be more pronounced in DED-LB than L-PBF due to the former's higher energy densities and slower cooling rates [84], which in martensitic steels cause more pronounced tempering-induced softening due to the formation of ε-, η-, and θ-carbides which relax the martensitic lattice via the diffusion of carbon out to these carbides. Higher energy densities and slower cooling rates in DED-LB also promote more dislocation recovery, recrystallization, and grain growth than in L-PBF, resulting in lower strength levels. While the process induced tempering reduces a martensitic steel's strength [85], Seede et al. [10] demonstrated that some of this loss in strength can be recovered in L-PBF AF9628 by imposing secondary heat treatments after printing (Table 6), and this should also be true for DED-LB AF9628.

However, it was discovered in this work that the discrepancy in strength in AF9628 between the L-PBF case is also somewhat attributable to the final composition of the printed parts. In this regard, notice the carbon (C) contents listed in Table 1 (and Fig. 18) for the three conditions – wrought AF9628, L-PBF AF9628, and DED-LB AF9628. Here, C content was lowered from 0.29 wt. % in wrought AF9628 to 0.23 wt. % in L-PBF AF9628 to, finally, 0.16 wt. % in DED-LB AF9628 due to the decarburization during printing. As shown in Table 1, in comparing the 'Powder' vs. 'As-Printed' columns showing relative compositional measurements, C losses were greater in DED-LB than in L-PBF, as both began at about 0.25 or 0.26 wt. % C. With this in mind, it is evident that C loss was most pronounced in DED-LB, partially explaining its lower strength levels compared to L-PBF AF9628. In this regard, C appears to evaporate more readily in DED-LB than in L-PBF due to the higher powers and slower speeds (i.e., higher linear energy densities) used in the former. In addition to carbon losses, Table 1 also shows that other elements were also evaporated, reducing the overall solid solution strengthening in DED-LB AF9628. Only Cr content remained constant for DED-LB AF9628, the reason for which is not clear.

5.2. Selection of initial powder composition

Following Figs. 13 and 18, DED-LB is capable of printing AF9628 AHSS to near full (> 99 %) density and excellent mechanical properties ($\sigma_{UTS} > 1.2$ GPa, $\varepsilon_f > 10$ % from Table 6) via the use of the DED-LB Process Optimization Framework, yet further improvements can be made to close the gap in properties between the wrought alloy and those printed using DED-LB. This gap mainly originates from combinations of extra tempering, larger prior austenite grain and martensite lath sizes, and carbon losses during printing due to DED-LB's higher energy densities versus L-PBF [20]. Regarding the latter, initial powder compositions should be selected accordingly for each AM technology to successfully achieve targeted compositions which are capable of producing the desired mechanical properties. Such an approach should facilitate printing AHSSs to compositions and properties in the as-printed condition that more accurately resemble the wrought condition or, at least, are achievable via post-printing heat treatments.

In addition to significant losses in C content, the other elemental contents have also changed after DED-LB, such as Ni, Si, and Mn (Table 1). As such, designing AHSSs with modified chemistries that account for the compositional discrepancies in as-printed conditions in C and other elements is vital for facilitating the printing of products to target compositions with strength levels matching those of wrought alloys. With this in mind, the design of alloyed powders of AHSSs for AM is an important next step. Further research is needed regarding printing to the desired target compositions by utilizing alloyed powders specifically designed for the DED-LB method and its incurred elemental losses during printing.

5.3. Further improvements in DED-LB process optimization framework

To further improve upon the DED-LB Process Optimization Framework, a variety of suggestions are made in this section. First, as seen in Fig. 11, it is apparent that some porosity remained throughout the bulk samples, either located at the bottom of builds as a lack of fusion defect or infrequently throughout the builds as seemingly random spherical porosity. The former is probably attributable to either differences in substrate *SR*s, where too smooth a surface reduces wettability, or effects of the rapid cooling rate at the substrate in contrast to the rest of the build, which can sometimes reduce proclivity for fusion of layers. Regarding the random spherical porosity evident throughout the builds, these pores are most likely caused by gas entrapment due to their shape [20]. Gas entrapment can occur from several effects, such as slight deviations in mass flow during printing or melting/burrowing of spattered/unmelted particles – which trap gas at their interfaces – during

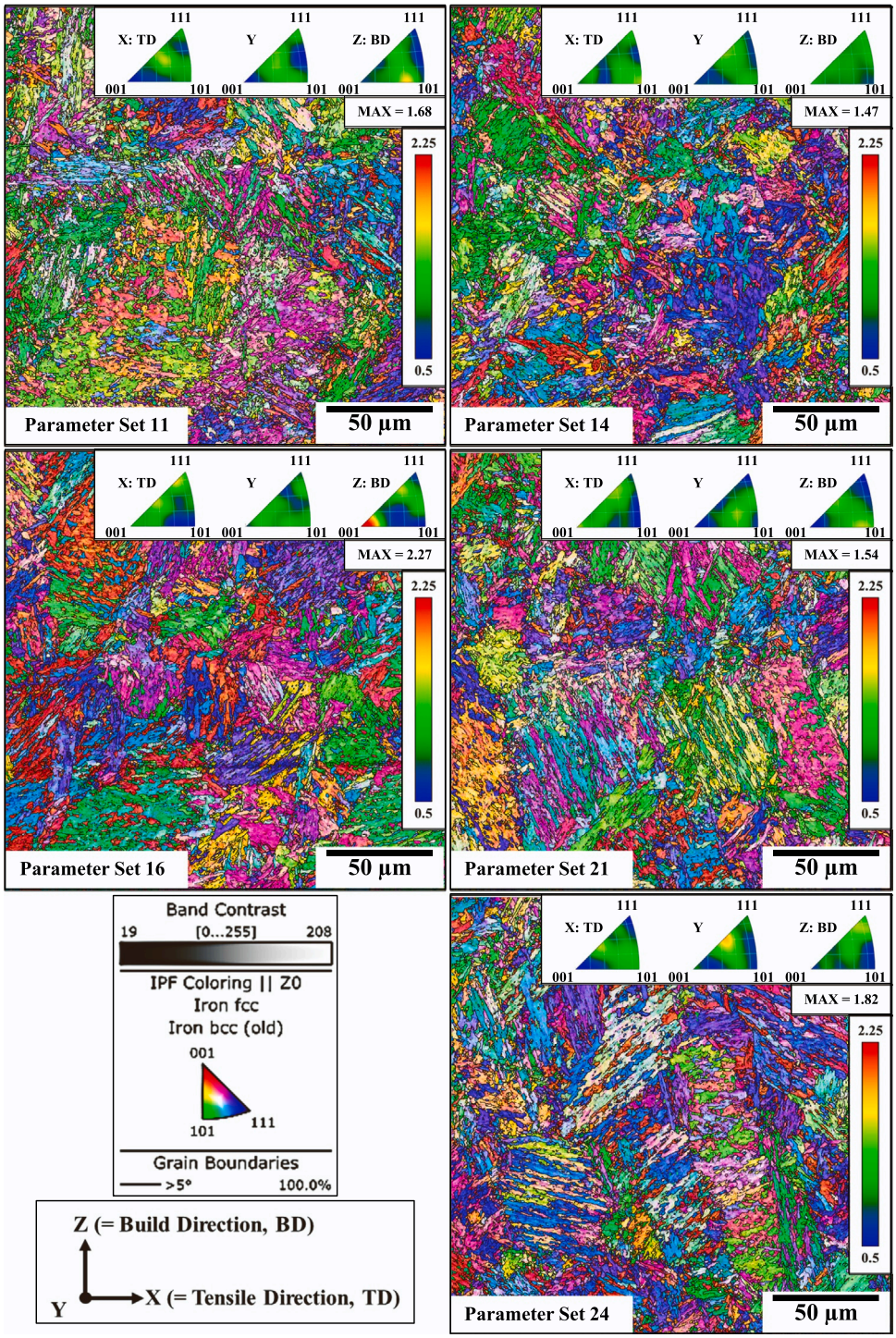

Fig. 15. EBSD inverse pole figure maps with band contrast showing martensitic lath boundaries, defined as the boundaries with misorientation angles >5°, for the five AF9628 tension blocks printed using DED-LB with the parameter sets 11, 14, 16, 21, and 24 (Table 5). Images were taken at the gage sections of the tension samples prior to testing. Inverse pole figure intensity maps along the three sample directions are also shown for each figure (Fig. 14).

printing of subsequent layers [79].

Two potential solutions for lack of fusion porosity are (1) increasing substrate *SR* and (2) applying substrate pre-heating during the earlier layers of a build to reduce the cooling rate and favor better bonding. To prevent porosity from gas entrapment, a laser rescan without any powder feeding could be completed in between layers. If rescanning power is set appropriately, it can favor smoothing of layers by melting of spattered particles [72] and the fusion and removal of voids without causing further issues, such as keyholing defects. Alternatively, Kumar et al. [86] showed via micro-CT scans that random spherical porosity could be reduced via using higher energy densities during printing. Thus, printing at higher energy densities than shown herein may reduce the spherical porosity, although it may introduce keyholing defects. Another potential solution is utilizing a better nozzle design, such as a coaxial nozzle [24,35–37] rather than the 4-nozzle system of the LENS MR-7 machine. A coaxial nozzle can offer better mass flow stability,

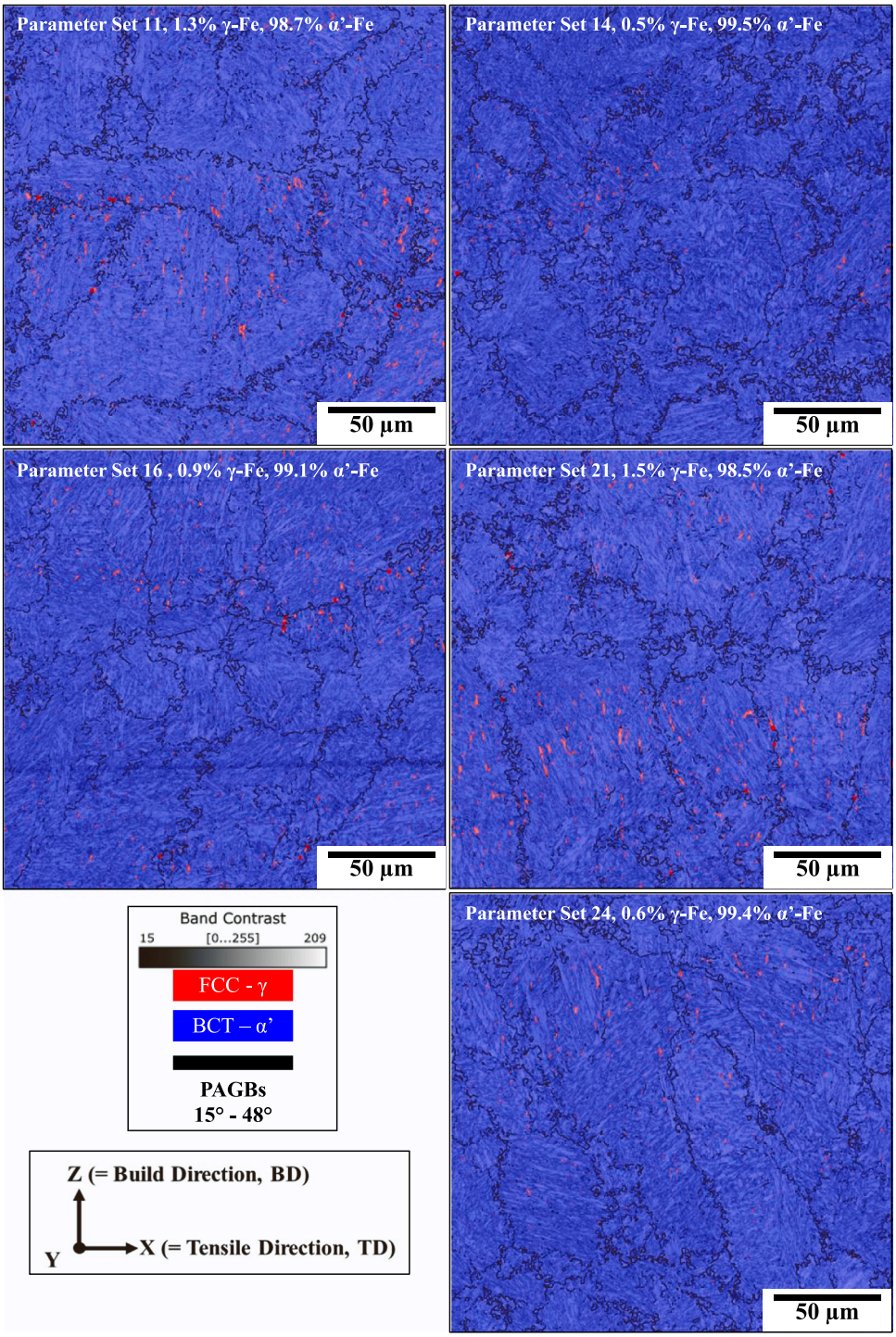

Fig. 16. EBSD phase maps with band contrast showing prior austenite grain boundaries (PAGBs) for the 5 AF9628 tension samples printed using DED-LB with the parameter sets 11, 14, 16, 21, and 24 (Table 5). Here, the PAG sizes are approximately equal for all conditions and appear elongated along the build direction. Images were taken at the gage sections of the tension samples prior to testing (Fig. 14).

thereby promoting more uniform melting and reducing the proclivity for random particle spattering and evaporation. Finally, the powder itself contributes to gas entrapment due to porosity formed during the atomization process; of course, completely removing this porosity would further reduce the randomized spherical porosity, but such a task is not feasible and essentially impossible to verify before printing. Overall, removing both types of porosity will improve the mechanical properties somewhat; however, as densities exceeded 99 %, improvements in mechanical properties are not expected to be very pronounced.

On a more industrial scale, further improvements can be made to increase volumetric build rates ($\dot{V}, cm^3/h$) and efficiencies (η_p, –) of AF9628 printed in DED-LB, defined according to Eqs. 7 and 8 [24,69], respectively, as follows:

$$\dot{V}(cm^3/h) = A_{Clad} * V \tag{7}$$

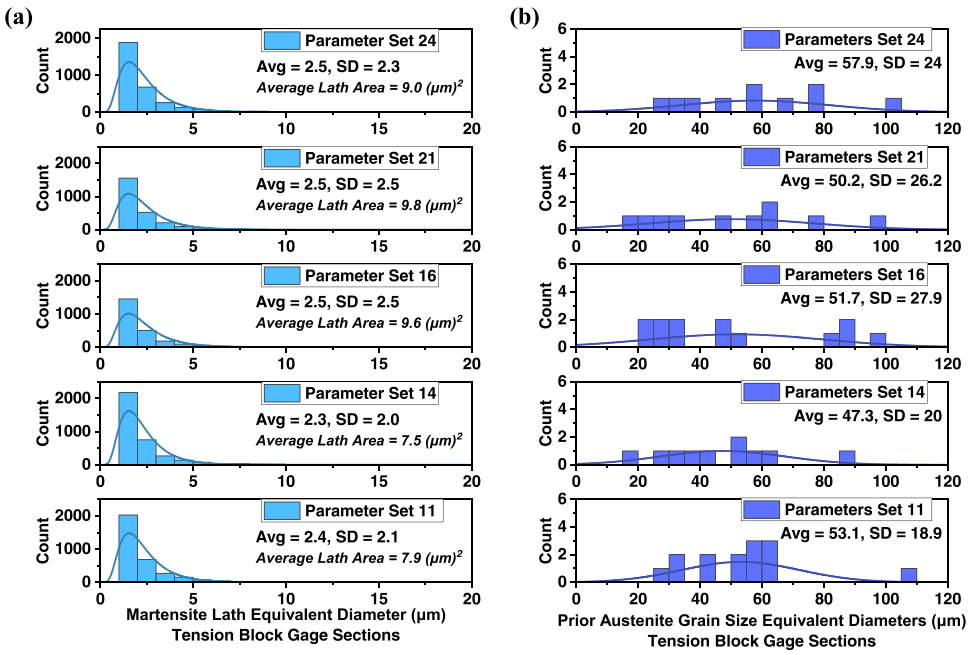

Fig. 17. (a) Martensitic lath equivalent diameter values and (b) prior austenite grain (PAG) sizes for the 5 tension blocks printed via DED-LB with the parameter sets 11, 14, 16, 21, and 24 (Table 5), showing general consistency in size across both. Consequently, the mechanical properties of all tension samples were similar. Note that the martensite laths equivalent diameters were calculated from individual lath areas measured in ImageJ, where boundaries were defined at 5° misorientation angles from the EBSD data. Average lath areas are written in (a) for completeness but are not shown in the graph. Also, PAGs were measured by imposing a 15–48° angle misorientation (as reported in [4,10,70]) and manually measuring the diameters via ImageJ.

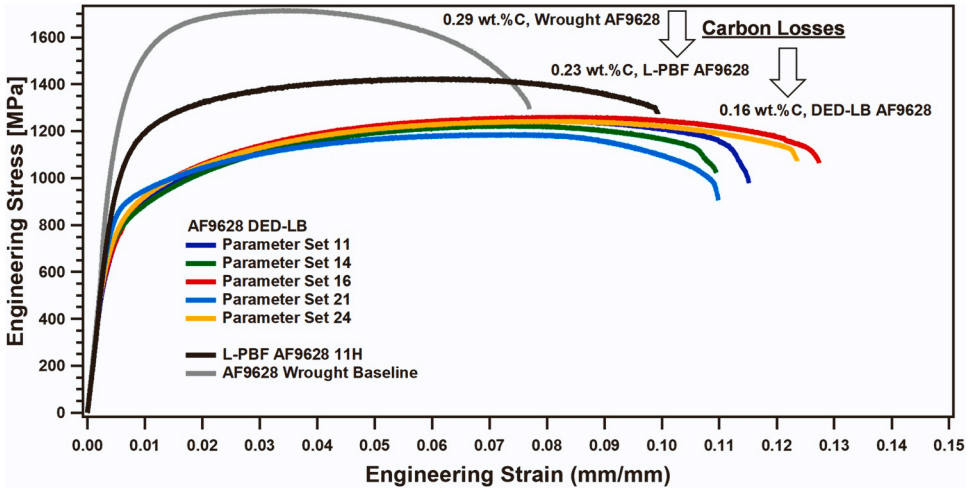

Fig. 18. Comparison plot for the AF9628 martensitic steel in a variety of processing conditions, such as DED-LB shown in this study versus L-PBF and Baseline wrought conditions. Overall, the loss in carbon content after L-PBF (to 0.23 wt. %) and DED-LB (to 0.16 wt. %) processing warrants the selection of new starting powder compositions that can arrive at the correct chemistries in the final parts after printing, in order to reach the appropriate strength limits comparable to the wrought AF9628 condition.

and

$$\eta_p(-) = A_{Clad}{}^{*}V{}^{*}\rho_p/\dot{m} \tag{8}$$

where ρ_p is the density of the powder being printed, and the other parameters are as defined previously. Essentially, these equations demonstrate that $\dot{V}$and η_p are both proportional to A_{Clad} and V, which would require, in turn, collectively higher P values to maintain optimal *Dilution* levels (20%–50%). Overall, increasing $\dot{V}$ has obvious practical benefits, i.e., faster print times and a more productive machine. Likewise, increasing η_p would reduce the waste of powder, which cannot be recycled very easily in DED-LB. It is worth mentioning that $\dot{V}$ could be considered relatively slow in the present work, at below 10 cm^3/h. Both $\dot{V}$ and η_p can be improved with different nozzle designs that can capture more powder [76]. Overall, collectively increasing the P, V, and $\dot{m}$ parameter levels in conjunction with improved powder flow dynamics via a coaxial powder nozzle should drastically improve both metrics and perhaps even reduce the random gaseous porosity as well.

6. Summary and conclusions

The present work introduced a DED-LB Process Optimization Framework which is summarized in Fig. 19. This framework can be utilized to fabricate near full (> 99 %) density parts of AF9628 martensitic steel, an AHSS, producing excellent strength and ductility levels (σ_{UTS} > 1.2 GPa, ε_f >10 %), and it can be applied easily to other metal alloy systems. Major findings can be summarized as follows:

1. The effects of several DED-LB printing parameters on the print quality of single tracks, bulk builds, and tension samples were analyzed in depth. The most ideal print parameters were identified, while the parameters that should be held constant were also determined.
2. A variety of printability maps were constructed from single-track characterization results. Contour maps of linear energy density ($LED = P/V$) vs. mass flow rate ($\dot{m}$) and laser power (P) vs. mass deposition rate ($MDR = \dot{m}/V$) plotted against single-track geometrical features provided a detailed understanding of print parameter effects on single-track H, D, W , A_{Clad}, A_{Melt}, *Dilution*, SR, and α.

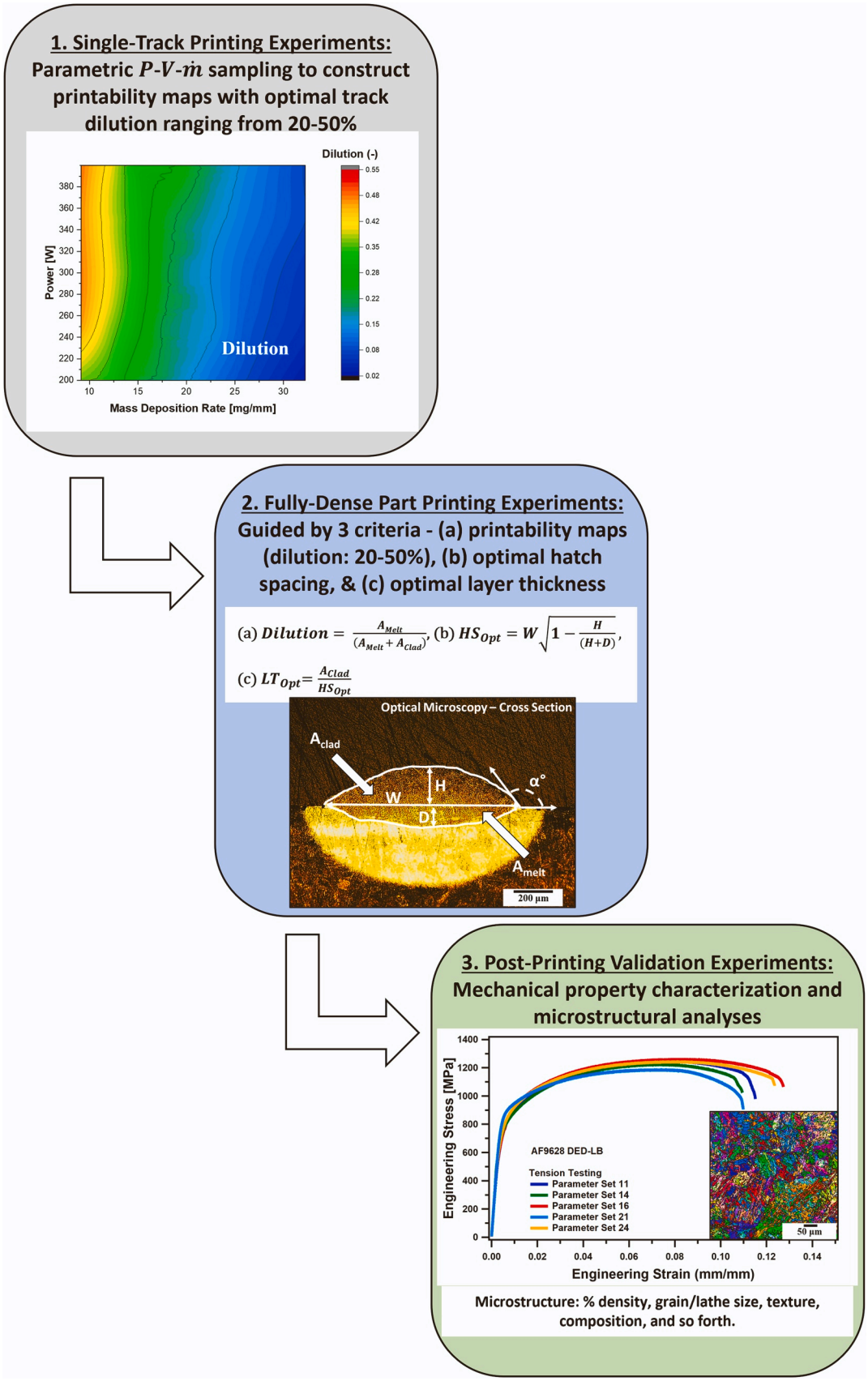

Fig. 19. The experimental flow chart for the DED-LB Process Optimization Framework introduced here, showing three main steps required to print a new material to full density and excellent mechanical performance.

Additionally, statistical models were constructed which indicated the effects of different print parameters and their interactions on the single-track geometries.

3. Parametric *P-V-ṁ* single-track experiments were used to construct printability maps with optimal *Dilutions* ranging between 20% and 50%. Here, geometries of single tracks were utilized to construct criteria for optimally setting hatch spacing (*HS*) and layer thickness (*LT*) for given *P-V-ṁ* combinations to favor maximal density in bulk parts. These printability maps, by showing the *Dilution*, HS_{opt}, and LT_{Opt} values altogether, enabled printing a specific parameter set combination to near full (> 99 %) density without requiring additional experiments.
4. The tensile responses of printed bulk samples were excellent (σ_{UTS} > 1.2 GPa, ε_f > 10 %). Also, general consistency in both strength and ductility was seen across the different parameter sets, which is difficult to achieve in DED-LB. Microstructural analyses of the 5 tension samples also demonstrated that DED-LB produced parts with similar martensite lath and PAG sizes regardless of the unique parameter combinations for each sample. Thus, DED-LB can produce consistent mechanical properties and microstructural refinement levels when the DED-LB Process Optimization Framework is applied to AHSSs such as AF9628.
5. Lower strengths compared to the wrought and L-PBF AF9628 conditions were partly attributable to the resultant larger grain sizes, extra tempering, and more pronounced carbon losses during DED-LB. The carbon losses indicate that the design of new powders specifically for DED-LB is an important next step for this technology.
6. Overall, the DED-LB Process Optimization Framework developed herein should further the ability to print new alloys and novel materials such as functionally graded parts to near full (> 99 %) density and excellent mechanical performance comparable to the wrought products.

CRediT authorship contribution statement

Matthew W. Vaughan: Conceptualization, Methodology, Software, Formal Analysis, Data Curation, Writing (Original Draft, Review, & Editing), Visualization | **Michael Elverud**: Methodology, Software | **Jiahui Ye**: Software, Visualization, Formal Analysis | **Raiyan Seede**: Formal Analysis | **Sean Gibbons, Philip Flater, B. Gaskey**: Resources, Supervision, Writing (Review & Editing) | **R. Arroyave, A. Elwany**: Conceptualization, Supervision, Writing (Review & Editing) | **I. Karaman**: Conceptualization, Methodology, Funding Acquisition, Supervision, Project Administration, Writing (Review & Editing).

Declaration of competing interest

The authors declare that they have no known competing financial interests or personal relationships that could have appeared to influence the work reported in this paper.

Data availability

Data will be made available on request.

Acknowledgments

This research was funded by the U.S. Air Force Research Laboratory through the Grant number FA8651-19-1-0005. AE acknowledges support from NSF under award CMMI-1846676.

References

[1] D. Coldewey, Space X's Starship goes sci-fi shiny with stainless steel skin, 2018. https://techcrunch.com/2018/12/26/spacexs-starship-goes-sci-fi-shiny-with-stainless-steel-skin/. (Accessed September 2022).
[2] R.A. Howell, Microstructural influence on dynamic properties of age hardenable FeMnAl alloys, Missouri University of Science & Technology, Ph.D. Dissertation, 2009.
[3] M. Brain, How Bunker Busters Work 2003. https://science.howstuffworks.com/bunker-buster.htm. (Accessed September 2022).
[4] M. Vaughan, P. Samimi, S. Gibbons, R. Abrahams, R. Harris, R. Barber, I. Karaman, Exploring performance limits of a new martensitic high strength steel by ausforming via equal channel angular pressing, Scr. Mater. 184 (2020) 63–69.
[5] J. Zhao, Z. Jiang, Thermomechanical processing of advanced high strength steels, Prog. Mater. Sci. (2018) 174–242.
[6] WorldAutoSteel, Tesla Takes Advantage of Steel Strength for Cybertruck Exoskeleton, 2020. https://www.worldautosteel.org/why-steel/steel-muscle-in-new-vehicles/tesla-cybertruck/. (Accessed September 2022).
[7] R.A. Abrahams, Low Alloy High Performance Steel, U.S. Patent and Trademark Office, 2019, Application No: 15/160,221, Patent No: 10,450,621.
[8] R. Seede, D. Shoukr, B. Zhang, A. Whitt, S. Gibbons, P. Flater, A. Elwany, R. Arroyave, I. Karaman, An ultra-high strength martensitic steel fabricated using selective laser melting additive manufacturing: densification, microstructure, and mechanical properties, Acta Mater. 186 (2020) 199–214.
[9] A. Elwany, I. Karaman, R. Arróyave, R. Seede, B. Zhang, L. Johnson, An integrated framework for assessing the printability of metallic materials and alloys using laser powder bed fusion additive manufacturing, U. S. Pat. Trademark Off. (2022). Application No: 17/500004.
[10] R. Seede, B. Zhang, A. Whitt, S. Picak, S. Gibbons, P. Flater, A. Elwany, R. Arroyave, I. Karaman, Effect of heat treatments on the microstructure and mechanical properties of an ultra-high strength martensitic steel fabricated via laser powder bed fusion additive manufacturing, Addit. Manuf. 47 (2021), 102255.
[11] K.C. Atli, H.M. Boon, R. Seede, B. Zhang, A. Elwany, R. Arroyave, I. Karaman, Laser-based additive manufacturing of a binary Ni-5 wt%Nb alloy, J. Manuf. Process. 62 (2021) 720–728.
[12] L. Johnson, M. Mahmoudi, B. Zhang, R. Seede, X.Q. Huang, J.T. Maier, H.J. Maier, I. Karaman, A. Elwany, R. Arroyave, Assessing printability maps in additive manufacturing of metal alloys, Acta Mater. 176 (2019) 199–210.
[13] L. Xue, K.C. Atli, S. Picak, C. Zhang, B. Zhang, A. Elwany, R. Arroyave, I. Karaman, Controlling martensitic transformation characteristics in defect-free NiTi shape memory alloys fabricated using laser powder bed fusion and a process optimization framework, Acta Mater. 215 (2021).
[14] L. Xue, K.C. Atli, C. Zhang, N. Hite, A. Srivastava, A.C. Leff, A.A. Wilson, D. J. Sharar, A. Elwany, R. Arroyave, I. Karaman, Laser powder bed fusion of defect-free NiTi shape memory alloy parts with superior tensile superelasticity, Acta Mater. 229 (2022).
[15] B. Zhang, R. Seede, A. Whitt, D. Shoukr, X.Q. Huang, I. Karaman, R. Arroyave, A. Elwany, A printability assessment framework for fabricating low variability nickel-niobium parts using laser powder bed fusion additive manufacturing, Rapid Prototyp. J. 27 (9) (2021) 1737–1748.
[16] B. Zhang, R. Seede, L. Xue, K.C. Atli, C. Zhang, A. Whitt, I. Karaman, R. Arroyave, A. Elwany, An efficient framework for printability assessment in Laser Powder Bed Fusion metal additive manufacturing, Addit. Manuf. 46 (2021).
[17] C. Zhang, H. Ozcan, L. Xue, K.C. Atli, R. Arroyave, I. Karaman, A. Elwany, On the effect of scan strategies on the transformation behavior and mechanical properties of additively manufactured NiTi shape memory alloys, J. Manuf. Process. 84 (2022) 260–271.
[18] C. Zhang, L. Xue, K.C. Atli, R. Arroyave, I. Karaman, A. Elwany, On the fabrication of defect-free nickel-rich nickel-titanium parts using laser powder bed fusion, J. Manuf. Sci. Eng. -Trans. Asme 144 (9) (2022).
[19] C. Zhang, L. Xue, S.A. Pestka, M. Ranaiefar, K.C. Atli, P. Honarmandi, R. Arroyave, I. Karaman, A. Elwany, Processing parameters and martensitic phase transformation relationships in near defect-free additively manufactured NiTiHf high temperature shape memory alloys, Mater. Des. 222 (2022).
[20] T. DebRoy, H. Wei, J. Zuback, T. Mukherjee, J. Elmer, J. Milewski, A.M. Beese, A. Wilson-Heid, A. De, W. Zhang, Additive manufacturing of metallic components–process, structure and properties, Prog. Mater. Sci. 92 (2018) 112–224.
[21] C. Atwood, M. Griffith, L. Harwell, E. Schlienger, M. Ensz, J. Smugeresky, T. Romero, D. Greene, D. Reckaway, Laser engineered net shaping (LENS™): a tool for direct fabrication of metal parts, International Congress on Applications of Lasers & Electro-optics, Laser Inst. Am. (1998) E1–E7.
[22] Z. Liu, B. He, T. Lyu, Y. Zou, A review on additive manufacturing of titanium alloys for aerospace applications: directed energy deposition and beyond Ti-6Al-4V, JOM 73 (6) (2021) 1804–1818.
[23] D. Herzog, V. Seyda, E. Wycisk, C. Emmelmann, Additive manufacturing of metals, Acta Mater. 117 (2016) 371–392.
[24] B. Bax, R. Rajput, R. Kellet, M. Reisacher, Systematic evaluation of process parameter maps for laser cladding and directed energy deposition, Addit. Manuf. 21 (2018) 487–494.
[25] P. Vetter, J. Fontaine, T. Engel, L. Lagrange, T. Marchione, Characterization of laser-material interaction during laser cladding process, WIT Trans. Eng. Sci. 2 (1993).
[26] J. Mazumder, J. Choi, K. Nagarathnam, J. Koch, D. Hetzner, The direct metal deposition of H13 tool steel for 3-D components, JOM 49 (5) (1997) 55–60.
[27] J. Bennett, D. Garcia, M. Kendrick, T. Hartman, G. Hyatt, K. Ehmann, F. You, J. Cao, Repairing automotive dies with directed energy deposition: industrial application and life cycle analysis, J. Manuf. Sci. Eng. 141 (2) (2019).
[28] A. Saboori, A. Aversa, G. Marchese, S. Biamino, M. Lombardi, P. Fino, Application of directed energy deposition-based additive manufacturing in repair, Appl. Sci. 9 (16) (2019) 3316.

[29] S.M. Thompson, L. Bian, N. Shamsaei, A. Yadollahi, An overview of direct laser deposition for additive manufacturing; part i: transport phenomena, modeling and diagnostics, Addit. Manuf. 8 (2015) 36–62.
[30] C. Wang, P. Zhang, K. Zhang, C. Wang, A novel process parameter screening strategy by comprehensively consideration of powder separation, defects and power consumption when fabricating FGM using laser metal deposition, J. Clean. Prod. 278 (2021), 123274.
[31] A. Reichardt, A.A. Shapiro, R. Otis, R.P. Dillon, J.P. Borgonia, B.W. McEnerney, P. Hosemann, A.M. Beese, Advances in additive manufacturing of metal-based functionally graded materials, Int. Mater. Rev. 66 (1) (2021) 1–29.
[32] H. Fayazfar, M. Salarian, A. Rogalsky, D. Sarker, P. Russo, V. Paserin, E. Toyserkani, A critical review of powder-based additive manufacturing of ferrous alloys: Process parameters, microstructure and mechanical properties, Mater. Des. 144 (2018) 98–128.
[33] T. Eagar, N. Tsai, Temperature fields produced by traveling distributed heat sources, Weld. J. 62 (12) (1983) 346–355.
[34] X. He, J. Mazumder, Transport phenomena during direct metal deposition, J. Appl. Phys. 101 (5) (2007), 053113.
[35] S. Wen, Y. Shin, J. Murthy, P. Sojka, Modeling of coaxial powder flow for the laser direct deposition process, Int. J. Heat. Mass Transf. 52 (25–26) (2009) 5867–5877.
[36] S. Wen, Y.C. Shin, Modeling of transport phenomena during the coaxial laser direct deposition process, J. Appl. Phys. 108 (4) (2010), 044908.
[37] I. Gibson, D. Rosen, B. Stucker, M. Khorasani, Additive Manufacturing Technologies, Springer 2014.
[38] A.J. Pinkerton, Advances in the modeling of laser direct metal deposition, J. Laser Appl. 27 (S1) (2015), S15001.
[39] S. Kumar, S. Roy, Development of theoretical process maps to study the role of powder preheating in laser cladding, Comput. Mater. Sci. 37 (4) (2006) 425–433.
[40] W. Steen, V.M. Weerasinghe, P. Monson, Some aspects of the formation of laser clad tracks, High Power Lasers and Their Industrial Applications, Int. Soc. Opt. Photonics (1986) 226–234.
[41] L. Costa, I. Felde, T. Réti, Z. Kálazi, R. Colaço, R. Vilar, B. Verő, A simplified semi-empirical method to select the processing parameters for laser clad coatings, Mater. Sci. Forum, Trans. Tech. Publ. (2003) 385–394.
[42] V. Ocelík, U. De Oliveira, M. De Boer, J. De Hosson, Thick Co-based coating on cast iron by side laser cladding: Analysis of processing conditions and coating properties, Surf. Coat. Technol. 201 (12) (2007) 5875–5883.
[43] H. El Cheikh, B. Courant, S. Branchu, J.-Y. Hascoet, R. Guillén, Analysis and prediction of single laser tracks geometrical characteristics in coaxial laser cladding process, Opt. Lasers Eng. 50 (3) (2012) 413–422.
[44] M. Erfanmanesh, H. Abdollah-Pour, H. Mohammadian-Semnani, R. Shoja-Razavi, An empirical-statistical model for laser cladding of WC-12Co powder on AISI 321 stainless steel, Opt. Laser Technol. 97 (2017) 180–186.
[45] P. Balu, P. Leggett, S. Hamid, R. Kovacevic, Multi-response optimization of laser-based powder deposition of multi-track single layer hastelloy C-276, Mater. Manuf. Process. 28 (2) (2013) 173–182.
[46] A. Kaplan, G. Groboth, Process analysis of laser beam cladding, J. Manuf. Sci. Eng. 123 (4) (2001) 609–614.
[47] W. Zhang, B. Zhang, H. Xiao, H. Yang, Y. Wang, H. Zhu, A layer-dependent analytical model for printability assessment of additive manufacturing copper/steel multi-material components by directed energy deposition, Micromachines 12 (11) (2021) 1394.
[48] F. Mazzucato, A. Aversa, R. Doglione, S. Biamino, A. Valente, M. Lombardi, Influence of process parameters and deposition strategy on laser metal deposition of 316L powder, Metals 9 (11) (2019) 1160.
[49] K.D. Traxel, D. Malihi, K. Starkey, A. Bandyopadhyay, Model-driven directed-energy-deposition process workflow incorporating powder flowrate as key parameter, Manuf. Lett. 25 (2020) 88–92.
[50] J. Shao, G. Yu, X. He, S. Li, Z. Li, X. Wang, Process maps and optimal processing windows based on three-dimensional morphological characteristics in laser directed energy deposition of Ni-based alloy, Opt. Laser Technol. 142 (2021), 107162.
[51] Z. Sun, W. Guo, L. Li, In-process measurement of melt pool cross-sectional geometry and grain orientation in a laser directed energy deposition additive manufacturing process, Opt. Laser Technol. 129 (2020), 106280.
[52] A. Jinoop, C. Paul, S. Mishra, K. Bindra, Laser additive manufacturing using directed energy deposition of inconel-718 wall structures with tailored characteristics, Vacuum 166 (2019) 270–278.
[53] F.M. Sciammarella, B. Salehi Najafabadi, Processing parameter DOE for 316L using directed energy deposition, J. Manuf. Mater. Process. 2 (3) (2018) 61.
[54] M. Ansari, R.S. Razavi, M. Barekat, An empirical-statistical model for coaxial laser cladding of NiCrAlY powder on Inconel 738 superalloy, Opt. Laser Technol. 86 (2016) 136–144.
[55] D.-R. Eo, S.-H. Park, J.-W. Cho, Controlling inclusion evolution behavior by adjusting flow rate of shielding gas during direct energy deposition of AISI 316 L, Addit. Manuf. 33 (2020), 101119.
[56] W. Jeong, Y.-S. Kwon, D. Kim, Three-dimensional printing of tungsten structures by directed energy deposition, Mater. Manuf. Process. 34 (9) (2019) 986–992.
[57] G. Zhu, D. Li, A. Zhang, G. Pi, Y. Tang, The influence of laser and powder defocusing characteristics on the surface quality in laser direct metal deposition, Opt. Laser Technol. 44 (2) (2012) 349–356.
[58] Z. Liu, H. Kim, W. Liu, W. Cong, Q. Jiang, H. Zhang, Influence of energy density on macro/micro structures and mechanical properties of as-deposited Inconel 718 parts fabricated by laser engineered net shaping, J. Manuf. Process. 42 (2019) 96–105.
[59] H. El Cheikh, B. Courant, S. Branchu, X. Huang, J.-Y. Hascoët, R. Guillén, Direct Laser Fabrication process with coaxial powder projection of 316L steel. Geometrical characteristics and microstructure characterization of wall structures, Opt. Lasers Eng. 50 (12) (2012) 1779–1784.
[60] J. Wanni, J. Michopoulos, A. Achuthan, Influence of cellular subgrain feature on mechanical deformation and properties of directed energy deposited stainless steel 316 L, Addit. Manuf. 51 (2022), 102603.
[61] J. Choi, Y. Chang, Characteristics of laser aided direct metal/material deposition process for tool steel, Int. J. Mach. Tools Manuf. 45 (4–5) (2005) 597–607.
[62] C. Paul, H. Alemohammad, E. Toyserkani, A. Khajepour, S. Corbin, Cladding of WC–12 Co on low carbon steel using a pulsed Nd: YAG laser, Mater. Sci. Eng.: A 464 (1–2) (2007) 170–176.
[63] Y. Sun, M. Hao, Statistical analysis and optimization of process parameters in Ti6Al4V laser cladding using Nd: YAG laser, Opt. Lasers Eng. 50 (7) (2012) 985–995.
[64] K. Mahmood, A.J. Pinkerton, Direct laser deposition with different types of 316L steel particle: a comparative study of final part properties, Proc. Inst. Mech. Eng., Part B: J. Eng. Manuf. 227 (4) (2013) 520–531.
[65] D.-S. Shim, G.-Y. Baek, J.-S. Seo, G.-Y. Shin, K.-P. Kim, K.-Y. Lee, Effect of layer thickness setting on deposition characteristics in direct energy deposition (DED) process, Opt. Laser Technol. 86 (2016) 69–78.
[66] N. Yang, J. Yee, B. Zheng, K. Gaiser, T. Reynolds, L. Clemon, W. Lu, J. Schoenung, E. Lavernia, Process-structure-property relationships for 316L stainless steel fabricated by additive manufacturing and its implication for component engineering, J. Therm. Spray. Technol. 26 (4) (2017) 610–626.
[67] B. Babu, M. Muthukumaran, Optimization of direct laser deposition process for shot sleeves used in aluminium diecasting, Int. J. Latest Technol. Eng. Manag. Appl. Sci. (2018) 139–144.
[68] T. Bhardwaj, M. Shukla, C. Paul, K. Bindra, Direct energy deposition-laser additive manufacturing of titanium-molybdenum alloy: parametric studies, microstructure and mechanical properties, J. Alloy. Compd. 787 (2019) 1238–1248.
[69] U. De Oliveira, V. Ocelik, J. De Hosson, Analysis of coaxial laser cladding processing conditions, Surf. Coat. Technol. 197 (2–3) (2005) 127–136.
[70] J. Gyhlesten Back, G. Engberg, Investigation of parent austenite grains from martensite structure using EBSD in a wear resistant steel, Materials 10 (5) (2017) 453.
[71] I. Tabernero, A. Lamikiz, S. Martínez, E. Ukar, L.L. De Lacalle, Modelling of energy attenuation due to powder flow-laser beam interaction during laser cladding process, J. Mater. Process. Technol. 212 (2) (2012) 516–522.
[72] L.E. dos Santos Paes, M. Pereira, F.A. Xavier, W.L. Weingaertner, A.S.C. M. D'Oliveira, E.C. Costa, L.O. Vilarinho, A. Scotti, Understanding the behavior of laser surface remelting after directed energy deposition additive manufacturing through comparing the use of iron and Inconel powders, J. Manuf. Process. 70 (2021) 494–507.
[73] L. Xue, K. Atli, C. Zhang, N. Hite, A. Srivastava, A. Leff, A. Wilson, D. Sharar, A. Elwany, R. Arroyave, Laser powder bed fusion of defect-free NiTi shape memory alloy parts with superior tensile superelasticity, Acta Mater. 229 (2022), 117781.
[74] R. Seede, J. Ye, A. Whitt, W. Trehern, A. Elwany, R. Arroyave, I. Karaman, Effect of composition and phase diagram features on printability and microstructure in laser powder bed fusion: Development and comparison of processing maps across alloy systems, Addit. Manuf. 47 (2021), 102258.
[75] M. Liu, A. Kumar, S. Bukkapatnam, M. Kuttolamadom, A review of the anomalies in directed energy deposition (DED) processes & potential solutions-part quality & defects, Procedia Manuf. 53 (2021) 507–518.
[76] J.C. Haley, B. Zheng, U.S. Bertoli, A.D. Dupuy, J.M. Schoenung, E.J. Lavernia, Working distance passive stability in laser directed energy deposition additive manufacturing, Mater. Des. 161 (2019) 86–94.
[77] J. Metelkova, Y. Kinds, K. Kempen, C. de Formanoir, A. Witvrouw, B. Van Hooreweder, On the influence of laser defocusing in Selective Laser Melting of 316L, Addit. Manuf. 23 (2018) 161–169.
[78] S.J. Wolff, S. Lin, E.J. Faierson, W.K. Liu, G.J. Wagner, J. Cao, A framework to link localized cooling and properties of directed energy deposition (DED)-processed Ti-6Al-4V, Acta Mater. 132 (2017) 106–117.
[79] S.J. Wolff, H. Wu, N. Parab, C. Zhao, K.F. Ehmann, T. Sun, J. Cao, In-situ high-speed X-ray imaging of piezo-driven directed energy deposition additive manufacturing, Sci. Rep. 9 (1) (2019) 1–14.
[80] J.C. Haley, J.M. Schoenung, E. Lavernia, Observations of particle-melt pool impact events in directed energy deposition, Addit. Manuf. 22 (2018) 368–374.
[81] L.E. dos Santos Paes, M. Pereira, F.A. Xavier, W.L. Weingaertner, L.O. Vilarinho, Lack of fusion mitigation in directed energy deposition with laser (DED-L) additive manufacturing through laser remelting, J. Manuf. Process. 73 (2022) 67–77.
[82] A. Heralić, A.-K. Christiansson, B. Lennartson, Height control of laser metal-wire deposition based on iterative learning control and 3D scanning, Opt. Lasers Eng. 50 (9) (2012) 1230–1241.
[83] D. Zhang, A. Prasad, M.J. Bermingham, C.J. Todaro, M.J. Benoit, M.N. Patel, D. Qiu, D.H. StJohn, M. Qian, M.A. Easton, Grain refinement of alloys in fusion-based additive manufacturing processes, Metall. Mater. Trans. A 51 (9) (2020) 4341–4359.
[84] D. Feenstra, V. Cruz, X. Gao, A. Molotnikov, N. Birbilis, Effect of build height on the properties of large format stainless steel 316L fabricated via directed energy deposition, Addit. Manuf. 34 (2020), 101205.
[85] W.F. Smith, Structure and Properties of Engineering Alloys, McGraw-Hill 1993.
[86] S. Kumar, L. Marandi, V.K. Balla, S. Bysakh, D. Piorunek, G. Eggeler, M. Das, I. Sen, Microstructure–property correlations for additively manufactured NiTi based shape memory alloys, Materialia 8 (2019), 100456.